



Deposited via The University of Sheffield.

White Rose Research Online URL for this paper:

<https://eprints.whiterose.ac.uk/id/eprint/212986/>

Version: Accepted Version

Article:

Crocker, A.J., Naafs, B.D.A., Westerhold, T. et al. (2022) Astronomically controlled aridity in the Sahara since at least 11 million years ago. *Nature Geoscience*, 15 (8). pp. 671-676.
ISSN: 1752-0894

<https://doi.org/10.1038/s41561-022-00990-7>

This version of the article has been accepted for publication, after peer review (when applicable) and is subject to Springer Nature's AM terms of use, but is not the Version of Record and does not reflect post-acceptance improvements, or any corrections. The Version of Record is available online at: <http://dx.doi.org/10.1038/s41561-022-00990-7>

Reuse

Items deposited in White Rose Research Online are protected by copyright, with all rights reserved unless indicated otherwise. They may be downloaded and/or printed for private study, or other acts as permitted by national copyright laws. The publisher or other rights holders may allow further reproduction and re-use of the full text version. This is indicated by the licence information on the White Rose Research Online record for the item.

Takedown

If you consider content in White Rose Research Online to be in breach of UK law, please notify us by emailing eprints@whiterose.ac.uk including the URL of the record and the reason for the withdrawal request.

1 **Astronomically controlled aridity in the Sahara since at least**
2 **11 million years ago**

3 **Anya J. Crocker^{1,2,*}, B. David A. Naafs³, Thomas Westerhold⁴, Rachael H.**
4 **James¹, Matthew J. Cooper¹, Ursula Röhl⁴, Richard D. Pancost³, Chuang Xuan¹,**
5 **Colin P. Osborne², David J. Beerling², Paul A. Wilson¹**

6 ¹University of Southampton, Waterfront Campus, National Oceanography Centre
7 Southampton, SO14 3ZH, United Kingdom.

8 ²Department of Animal and Plant Sciences, University of Sheffield, Sheffield, S10
9 2TN, United Kingdom.

10 ³Organic Geochemistry Unit, School of Chemistry, School of Earth Sciences, and
11 Cabot Institute for the Environment, University of Bristol, Bristol, United Kingdom.

12 ⁴MARUM – Center for Marine Environmental Sciences, University of Bremen,
13 Leobener Strasse, 28359 Bremen, Germany.

14 * Correspondence to: anya.crocker@noc.soton.ac.uk

15

16 **Abstract**

17 **The Sahara is the largest hot desert on Earth. Yet, the timing of its inception and**
18 **its response to climatic forcing is debated, leading to uncertainty over the causes**
19 **and consequences of regional aridity. Here we present detailed records of**
20 **terrestrial inputs from Africa to North Atlantic deep-sea sediments, documenting**
21 **a long and sustained history of astronomically-paced oscillations between a**
22 **humid and arid Sahara from over 11 million years (Myr) ago. We show that**
23 **intervals of strong dust emissions from the heart of the continent predate both**
24 **the intensification of northern hemisphere glaciation and the oldest land-based**
25 **evidence for a Saharan Desert by millions of years. We find no simple long-term**
26 **gradational transition towards an increasingly arid climate state in northern**
27 **Africa, suggesting that aridity was not the primary driver of gradual Neogene**
28 **expansion of African savanna C₄ grasslands. Instead, insolation-driven wet-dry**
29 **shifts in Saharan climate were common over the last 11 Myr and we identify**
30 **three distinct stages in the sensitivity of this relationship. Our data provide**
31 **context for evolutionary outcomes on Africa, for example, we find that**
32 **astronomically-paced arid intervals predate the oldest fossil evidence of hominid**
33 **bipedalism by at least 4 Myr.**

34

35 **Main text**

36 Prominent from space, the Saharan desert is a vast, bare, intensely arid, dust-exporting
37 landscape that grew 10% in response to climatic forcing during the 20th century¹. A
38 recognisable Saharan desert is widely suggested to originate in the late Pliocene, ~2.6
39 Myr ago, coupled to the development of major continental ice sheets in the Northern

40 Hemisphere and their expansion during the mid-Pleistocene transition (ca. 1.2–0.6
41 Myr ago)^{2,3}. Yet, this interpretation has been challenged⁴, and evidence of Saharan
42 dust in ~4.8 Myr old Canary Island palaeosols⁵ and proposed aeolian dune deposits
43 from the Djurab of Chad dated to ~7 Myr ago⁶ hint at an earlier inception of desert
44 conditions. Weakening of the summer monsoon in climate model simulations of the
45 response to Tethys Sea closure is hypothesized⁷ to account for earlier desertification.
46 However, the significance of the fossil dunes is highly controversial⁸, estimated dates
47 of Tethys closure span more than 20 Myr^{9,10} and existing climate records are too
48 sparse to test these competing hypotheses for desert inception. Thus, the geological
49 history of the world's largest hot desert, which exerts a major influence on the Earth's
50 energy balance and global biogeochemical cycles, remains poorly constrained.

51

52 **Unearthing terrestrial climate history in marine sediments**

53 We investigated the evolution of African aridity and atmospheric dust export over the
54 last 11 Myr by developing continuous, high resolution and well-dated geochemical
55 records of terrigenous inputs from northern Africa to marine sediment archives. We
56 studied Ocean Drilling Project (ODP) Site 659 off Mauritania (Supplementary Figure
57 1), situated underneath the main modern Saharan dust plume. Pronounced cycles in
58 colour and lithology of Site 659 sediments record changes in terrigenous content and,
59 in the seminal study of Tiedemann et al.¹¹, these changes were quantified and used to
60 infer dust inputs and aridity change on Africa over the past 5 million years. Yet, that
61 hydroclimate reconstruction is now called into question for three reasons: First, distal,
62 fine-grained material, likely of riverine origin, also contributes to the lithogenic
63 fraction of sediment accumulating on the northwest African margin including Site

64 659^{12,13} (see Supplementary Information). Second, the proportion of terrigenous
65 material in marine sediments is also influenced by marine carbonate deposition and
66 dissolution, which may exert a significant control, particularly in Pliocene and
67 Miocene-aged sediments at Site 659^{14,15}. Third, dust supply to the atmosphere and
68 marine sediments is controlled not only by aridity but also wind strength¹⁶.

69

70 We used X-ray fluorescence (XRF) core scanning to both document dust
71 accumulation in the North Atlantic Ocean and infer African hydroclimate over the last
72 11 Myrs geochemically (Figure 1). Because dust flux estimates show a strong wind
73 strength dependence and can be biased by carbonate dissolution and rapid fluctuations
74 in sediment accumulation¹⁵, we use two geochemical ratios, $[Al+Fe]/[Si+K+Ti]$ and
75 $\ln[Zr/Rb]$, to reconstruct hydroclimate variability. High $[Al+Fe]/[Si+K+Ti]$ values are
76 associated with low inputs of Si-rich dust and more intense chemical weathering
77 under humid climates¹⁷ while high $\ln[Zr/Rb]$ values indicate dominance of coarse dust
78 over fine river clays¹². Crucially, these two ratios employ only lithophile elements and
79 so, unlike dust fluxes, they are independent of sea-floor carbonate dissolution and
80 dilution and show strong agreement with hydroclimate reconstructions based upon
81 deuterium isotopic signatures of plant waxes (Figure 2, Extended Data Figures 1–2
82 and Supplementary Information). Our dust flux reconstructions are similar to thorium-
83 normalization based estimates from nearby site MD03-2705¹⁵ (Extended Data Figure
84 3 and Supplementary Information) suggesting that, although the influence of dilution,
85 dissolution, rapid sedimentation rate fluctuations and sediment remobilisation cannot
86 be entirely ruled out, they are not likely main drivers of reconstructed dust fluxes at
87 Site 659.

88

89 Our high-resolution records (Figure 1) reveal a long history of repeated dramatic
90 shifts in hydroclimate between dry dusty conditions and more humid intervals
91 reaching back 11 Myrs. The most recent of these is the African Humid Period (AHP1)
92 in the early Holocene, when the Saharan landscape was well-vegetated and cross-cut
93 by a network of rivers and lakes^{13, 18-20} with abundant archaeological sites, some
94 adorned with rock art depictions of giraffe, elephant, hippopotamus and domesticated
95 cattle²¹. Throughout our record, dark terrigenous-rich sediment layers at Site 659 have
96 significantly higher $\ln[\text{Zr}/\text{Rb}]$ and lower $[\text{Al}+\text{Fe}]/[\text{Si}+\text{K}+\text{Ti}]$ values than pale layers
97 indicating that they contain a greater proportion of coarser grains, and have a
98 chemical signature approaching dust end-member values (Figure 3, Extended Data
99 Figure 4 and Supplementary Information). Thus, the dark layers consistently signify
100 high dust deposition linked to aridity over northern Africa rather than high riverine
101 sediment input or merely strong sea floor carbonate dissolution. Intervening paler
102 layers consistently record low $\ln[\text{Zr}/\text{Rb}]$ and high $[\text{Al}+\text{Fe}]/[\text{Si}+\text{K}+\text{Ti}]$, indicating far
103 less dusty conditions on Africa. Spectral analysis reveals that this climatic variability
104 is primarily paced by precession and obliquity, with a strong signature of eccentricity
105 only documented in the oldest (Miocene) part of our records (Extended Data Figures
106 5–6 and Supplementary Information).

107

108 **Long-lived pulsing of Saharan dust export**

109 We identify three distinct stages in the evolution of Saharan hydroclimate state over
110 the past 11 Myrs, separated by transitions with statistically significant shifts in central
111 tendency and dispersion in our datasets (Figure 1, Extended Data Figure 7 and
112 Supplementary Information). Stage I (>6.9 Myr ago) reveals astronomically-paced

113 development of arid and dust-producing regions on Africa from at least 11 Myr ago.
114 Pronounced dark sediment layers consistently show high $\ln[\text{Zr}/\text{Rb}]$ and low
115 $[\text{Al}+\text{Fe}]/[\text{Si}+\text{K}+\text{Ti}]$ values, confirming that these layers are, like those in the younger
116 part of the record, associated with aridity (Figure 3, Extended Data Figure 4). Both
117 $\ln[\text{Zr}/\text{Rb}]$ and $[\text{Al}+\text{Fe}]/[\text{Si}+\text{K}+\text{Ti}]$ values suggest that African climate was more arid
118 during the Late Miocene than the Pliocene, however estimated dust flux maxima are
119 lower. Given the importance of deflation-promoting high wind speeds (gustiness) in
120 dust transport, we attribute this result to warmer Miocene high latitudes weakening
121 latitudinal temperature gradients (Figure 1c), resulting in lower wind speeds and less
122 effective deflation and dust transport²²⁻²⁵. Nevertheless, our records document
123 substantial dust emissions that predate the oldest land-based evidence (~7 Myr ago)
124 for Miocene initiation of northern African hyperaridity⁶ by at least 4 Myr, and predate
125 Late Pliocene intensification of Northern Hemisphere Glaciation (iNHG)^{2,3} by at least
126 8 Myr.

127

128 A shift towards increased $[\text{Al}+\text{Fe}]/[\text{Si}+\text{K}+\text{Ti}]$ values followed by decreased $\ln[\text{Zr}/\text{Rb}]$
129 from ~6.9 Ma marks the transition into stage II (which covers the latest Miocene to
130 the late Pliocene, ~5.75–3.5 Ma), indicating wetter conditions with more fine-grained
131 sedimentary inputs (Figure 1f and g). Increasing variability in $[\text{Al}+\text{Fe}]/[\text{Si}+\text{K}+\text{Ti}]$,
132 $\ln[\text{Zr}/\text{Rb}]$ and dust fluxes is also recorded implying a heightened sensitivity of
133 northern African humidity to astronomical forcing, although cycle amplitudes may
134 also be more attenuated by bioturbation in Stage I where sedimentation rates are
135 lower (Supplementary Figure 2). Dust fluxes during stage II are lower during humid
136 events associated with insolation maxima but higher during arid insolation minima
137 than seen for equivalent forcing in stage I. We attribute this result to the development

138 of extensive Pliocene river systems and lakes (including Lake Chad which has a
139 Latest Miocene origin²⁶) during ‘wet orbits’ that, once desiccated, became dust-
140 producing hot-spots^{27,28} during succeeding ‘dry orbits’.

141

142 The transition to Stage III, which covers the last ~2.25 Myrs (early Pleistocene to
143 Recent) of African climate history, is characterized by a shift towards more arid
144 conditions (decreasing $[Al+Fe]/[Si+K+Ti]$ centred around 3.1 Ma) followed, ca. 400
145 kyr later, by increased mean values of $\ln[Zr/Rb]$ and dust fluxes (which also show
146 higher amplitude variability), closely contemporaneous with the intensification of
147 glacials as revealed by benthic oxygen isotope records²⁹ (Figure 1b). The highest dust
148 fluxes in our records during Stage III are consistent with the suggestion that the
149 growth of large continental ice sheets in the Northern Hemisphere promoted the
150 development of more arid and dusty conditions on Africa through steepening
151 latitudinal temperature gradients and strengthening winds^{3,30}.

152

153 **Consistency of source**

154 We investigated the source of terrigenous material accumulating at ODP Site 659 over
155 the last 11 Myr using radiogenic isotopes. Today, dust is generated widely across
156 three geochemically distinct northern African preferential source areas (PSAs)³¹.
157 Strontium and neodymium isotopic signatures of the lithogenic fraction of Site 659
158 sediments are remarkably consistent compared to the range in modern PSA signatures
159 and lie between those reported for the Central and currently undersampled Western
160 source regions³¹ (Figure 4). These results imply that the terrigenous source regions
161 remained broadly unchanged over the past 11 Myr and that variability in grain size is

162 not a major control on our data (Extended Data Figures 8–10 and Supplementary
163 Information). This observation, together with the high $\ln[\text{Zr}/\text{Rb}]$ and
164 $[\text{Al}+\text{Fe}]/[\text{Si}+\text{K}+\text{Ti}]$ values recorded during Miocene insolation minima, indicates that
165 dust-producing regions existed in the inland Sahara region and were activated by
166 astronomical forcing back to at least 11 Myr ago. We conclude that while iNHG in the
167 late Pliocene (~3.3–2.5 Myr ago) drove increased dust fluxes (Figure 1h), it was not
168 responsible for the inception of the Saharan desert.

169

170 **Rainfall climate, C₄ savannas and evolutionary outcomes**

171 Savannas dominated by C₄ grasses expanded extensively during the late Miocene^{32,33},
172 but the cause of this major reorganization of the terrestrial biosphere is controversial.
173 Both aridification and decreasing $p\text{CO}_2$ are proposed drivers of this grassland
174 ecosystem shift, aided by strong positive feedbacks associated with fire, and
175 regionally modified by latitude, altitude and rainfall seasonality³²⁻³⁷. To better
176 understand the potential role of hydroclimate variability in driving the expansion of
177 C₄ grasslands, we compare our geochemical datasets to stable carbon ($\delta^{13}\text{C}$) and
178 hydrogen (δD) isotope signatures of leaf wax long-chain *n*-alkanes at Site 659
179 (Figures 1d and 2). The carbon isotope signature of plant waxes is strongly controlled
180 by the photosynthetic pathway of the parent plant: *n*-alkanes from C₄ plants are
181 isotopically heavier ($-21.4\pm 2.2\text{‰}$) than C₃ plants ($-34.9\pm 2.7\text{‰}$)³⁸.

182

183 We find little similarity between the gradational expansion of C₄ grasses in northern
184 Africa and long-term hydroclimate trends (Figure 1). The plant wax records integrate
185 material from across a large source area that was dominated by C₄ vegetation during

186 the Quaternary^{39,40}, potentially contributing to the expression of only modest change
187 in *n*-alkane $\delta^{13}\text{C}$ in response to insolation forcing in the youngest part of the record.
188 Nevertheless, the hydroclimate signal in North Africa ($[\text{Al}+\text{Fe}]/\text{Si}+\text{K}+\text{Ti}$], $\ln[\text{Zr}/\text{Rb}]$
189 and *n*-alkane $\delta\text{D}^{36,39,40}$) is dominated by astronomical variability, while the vegetation
190 signal (*n*-alkane $\delta^{13}\text{C}^{36,39,40}$) is dominated by the gradual long-term trend that defines
191 the C₃-C₄ transition and is not replicated by the hydroclimate reconstructions (Figures
192 1 and 2, Supplementary Figure 3). Therefore, we find that a simple hydroclimate
193 driver cannot explain C₄ grassland expansion in northwest Africa through the
194 Neogene. A similar conclusion was reached by ref. 36. However, while that study
195 ruled out a hydroclimate control because of little inferred change in regional rainfall,
196 we document major changes in hydroclimate unaccompanied by a strong response in
197 C₄ plant dominance (Figure 2). This decoupling between aridity and C₃-C₄
198 composition does not rule out an influence of aridity on C₄ vegetation dominance, but
199 suggests that the relationship was not simple. An improved record of Neogene *p*CO₂
200 variability (Figure 1a) is needed to better understand coupling between global climate
201 state, hydroclimate and the rise of C₄ grasslands.

202

203 An inferred progressive aridification of Africa and spread of savanna ecosystems has
204 been linked to speciation and development of long-range mobility in hominins^{3, 41} and
205 extinction of many large mammals^{32,42}. Our long, detailed, continuous marine records
206 help to develop the environmental framework needed to assess these evolutionary
207 outcomes on land, including the hypothesized relationships between habitat instability
208 and development in hominins of characteristics that promote adaptability^{43,44}. We
209 highlight the longevity and primacy of the astronomical signal in controlling
210 hydroclimate in northern Africa. Our findings of three distinct phases in North

211 African hydroclimate, including relatively dry conditions during the warm Miocene,
212 suggest no simple escalation in aridity through the late Cenozoic associated with
213 global cooling, and argue against aridity as the primary driver of C₄ grassland
214 expansion. Our records show evidence of changes in mean state and/or amplitude of
215 variability in hydroclimate close to the oldest suggested fossil evidence of hominin
216 bipedalism⁴⁵ and the earliest records of the genus *Homo*⁴⁶ (Figure 1). However, the
217 confidence interval on the origination of the principal taxa, especially suggested
218 bipeds, is large, implying earlier emergence⁴⁷. New fossil finds will inevitably revise
219 the hominin chronology, enabling a stronger understanding of the evolutionary link to
220 climate. Meanwhile, our study reveals astronomically-paced dry and dusty conditions
221 on Africa long before both the oldest land-based evidence of a Saharan desert and the
222 intensification of Northern Hemisphere glaciation.

223

224 **Acknowledgments**

225 This research was funded through ERC advanced grant CDREG no. 322998 (D.J.B.)
226 and the Royal Society Challenge Grant CHG\R1\170054 (P.A.W.) and Wolfson Merit
227 Award WM140011 (P.A.W.). Additional funding came from University of
228 Southampton's GCRF strategic development fund grant 519016 (P.A.W. and A.J.C.),
229 advanced ERC grant T-GRES ref. 340923 (B.D.A.N. and R.D.P.) and a Royal Society
230 Tata University Research Fellowship (B.D.A.N.). We thank the Natural Environment
231 Research Council for partial funding of the mass spectrometry facilities at the
232 University of Bristol (contract no. R8/H10/63). Financial support was also received
233 from the Deutsche Forschungsgemeinschaft (DFG) (U.R. and T.W.) including project
234 242225091 (T.W).

235

236 This research used samples provided by (I)ODP, which was sponsored by the US
237 National Science Foundation and participating countries under management of Joint
238 Oceanographic Institutions, Inc. We thank Walter Hale, Holger Kuhlman and Alex
239 Wülbers of the Bremen Core Repository, and Rachael Kretsis James, Andrew
240 McCombie and Cat Evans for laboratory assistance, Angus Calder for discrete XRF
241 analysis and Vera Lukies for assistance with XRF core scanning. Biostratigraphic
242 information was provided by Jan Backman and Stefan Mulitza supplied the
243 geochemical endmember unmixing code. We thank David McGee, Jessica Tierney,
244 Tom Ezard, Clive Gamble, Alistair Pike, Katherine Grant, Sarah Feakins, Eelco
245 Rohling and Stefan Mulitza for discussions and feedback that helped to improve this
246 manuscript.

247

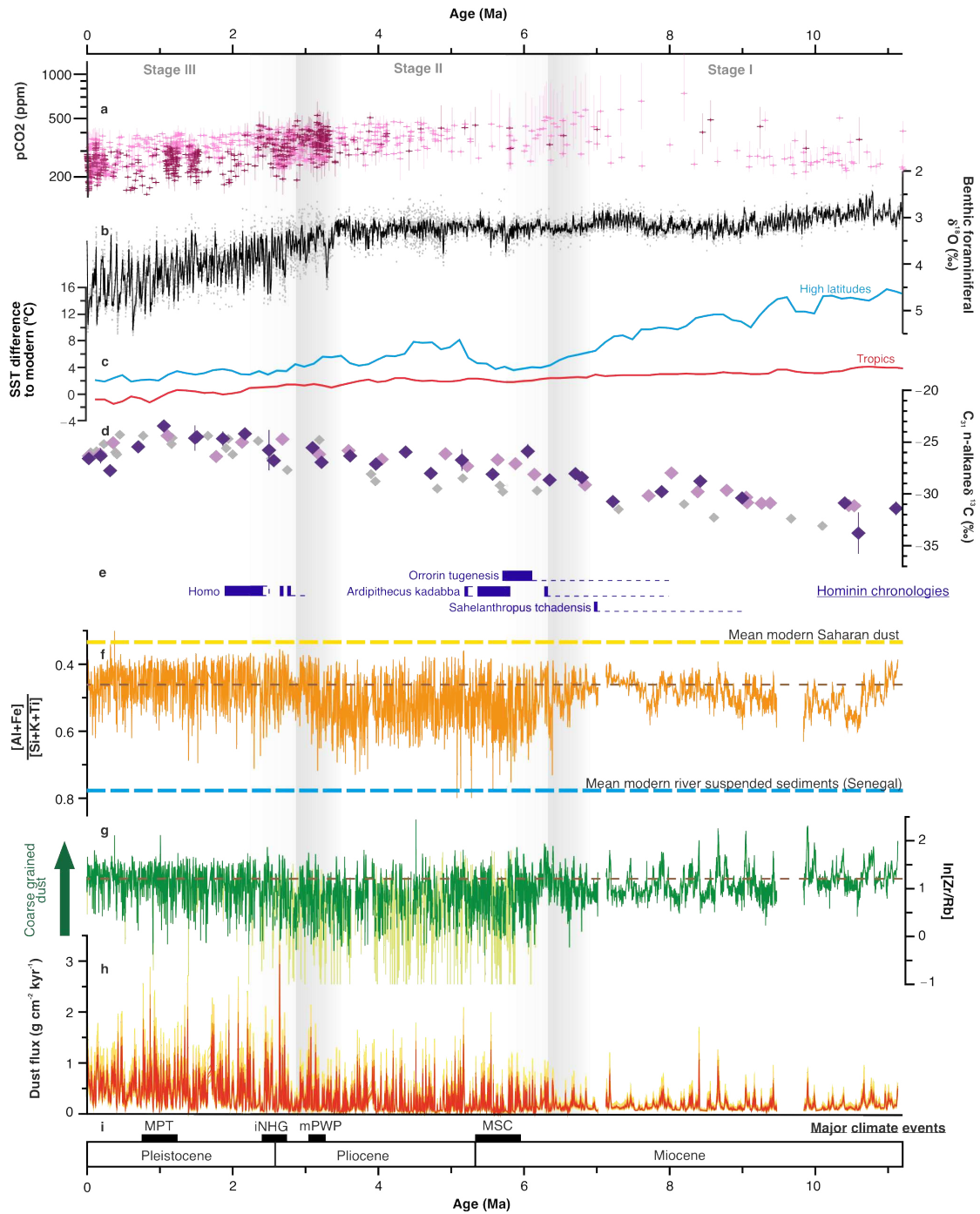
248 **Author contributions**

249 A.J.C., P.A.W., C.P.O. and D.J.B. designed the study. A.J.C. and T.W. performed the
250 XRF measurements and developed the age model. B.D.A.N. generated the *n*-alkane
251 $\delta^{13}\text{C}$ data and M.J.C. and A.J.C. generated the radiogenic isotope data. A.J.C.
252 performed the sediment endmember unmixing. A.J.C. and P.A.W. led the analysis and
253 interpretation of results with input from all authors. A.J.C., P.A.W., D.J.B. and C.P.O.
254 led the writing of the manuscript with contributions from all other authors.

255

256 **Competing interests**

257 The authors declare no competing interests.



259

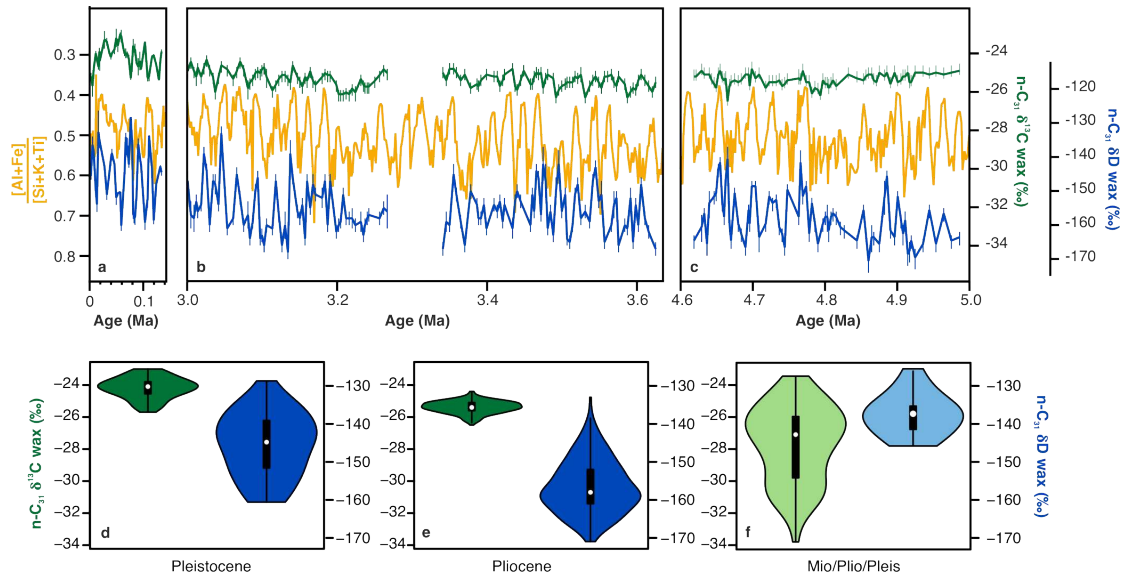
260 **Figure 1| African hydroclimate compared to global change over the past 11 Myr. a**

261 Atmospheric pCO_2 reconstructions (references in Supplementary Information),

262 purple: estimates from planktonic foraminiferal boron isotopic signatures, pink:

263 alkenone-derived estimates. **b** Cenozoic global reference benthic foraminifera oxygen

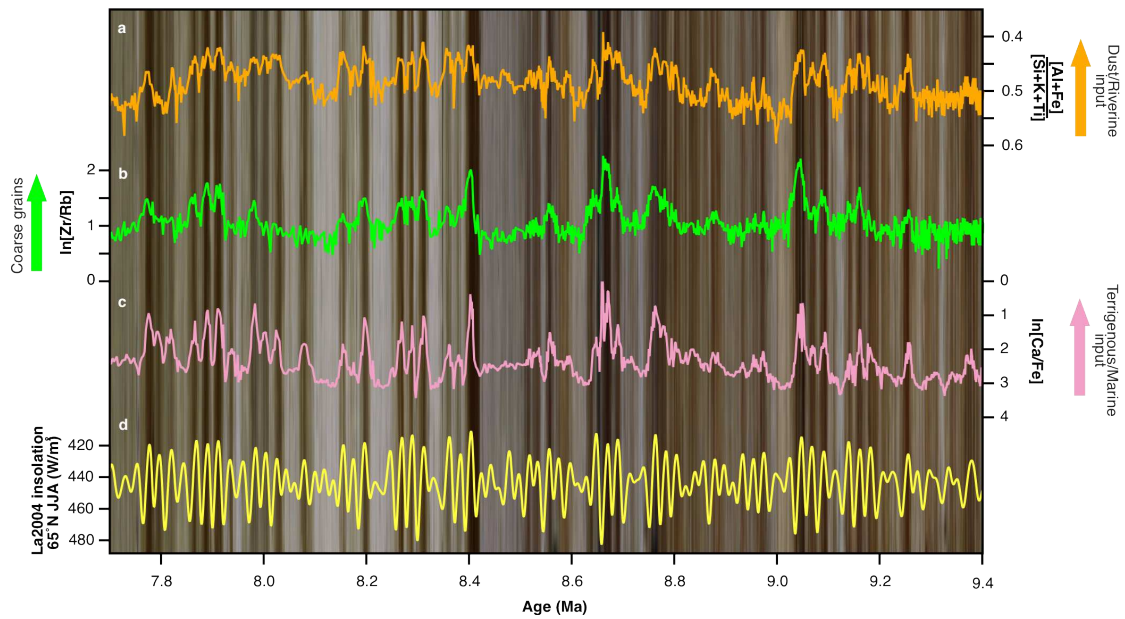
264 isotope dataset, with 20 kyr smoothing²⁹. **c** Regional stacks of sea surface temperature
265 difference to modern annual means²³, blue: >50°N, red: tropics. **d** $\delta^{13}\text{C}$ signature of *n*-
266 alkanes from Site 659 (dark purple: this study, light purple: ref. 36) and offshore E.
267 Africa⁴⁸ (grey). Error bars indicate 1σ . **e** Major events in hominid evolution. Solid
268 bars: taxon ranges, dashed lines: confidence interval on taxon origin⁴⁷. **f**
269 $[\text{Al}+\text{Fe}]/[\text{Si}+\text{K}+\text{Ti}]$ of calibrated elemental abundances. Modern endmember values
270 updated from ref. 17 (see Supplementary Information). Dashed line marks mean over
271 last 1 Myr. **g** $\ln[\text{Zr}/\text{Rb}]$ XRF core scan ratios. Dashed line marks mean over last 1
272 Myr. **h** Site 659 estimated dust flux (3pt smoothed). Median value in red; 1%, 5%,
273 25%, 75%, 95% and 99% percentiles also shown in shades of orange/yellow. **i** Major
274 global climate events. MPT: mid-Pleistocene transition, iNHG: intensification of
275 Northern Hemisphere glaciation, mPWP: mid-Pliocene warm period, MSC:
276 Messinian Salinity Crisis. Vertical grey shading indicates transitions between climate
277 stages.
278



280

281 **Figure 2| Relationship between lithophile element ratios and hydrogen and**
 282 **carbon isotopic compositions of plant waxes at Site 659. a** Last glacial cycle, **b** late
 283 Pliocene, **c** early Pliocene. $[Al+Fe]/[Si+K+Ti]$ of bulk sediment in orange (this study).
 284 Leaf wax C_{31} n -alkane $\delta^{13}C$ data in green^{39,40} and δD in blue^{39,40}, error bars mark 1
 285 standard deviation. High $[Al+Fe]/[Si+K+Ti]$ and low n -alkane δD values both
 286 indicate more humid conditions. **d-f** Violin plots indicating the distribution of leaf
 287 wax C_{31} n -alkane $\delta^{13}C$ (green) and δD (blue) data in high-resolution snapshots in the
 288 Late Quaternary (**d**) and Pliocene (**e**) (data from refs. 39 and 40), and low-resolution
 289 records covering the last 11 Myr (**f**, data from this study and ref. 36). White dots
 290 indicate median values, black rectangles indicate interquartile range.

291



292

293

Figure 3| Strong response of African hydroclimate to astronomical forcing

294

recorded at Site 659. Example from the late Miocene. **a** $[Al+Fe]/[Si+K+Ti]$ of

295

calibrated elemental abundances. **b,c** $\ln[Zr/Rb]$ and $\ln[Ca/Fe]$ XRF core scan ratios. **d**

296

Summer insolation at $65^{\circ}N$ ⁴⁹. Background colour shows the composited sediment

297

core image. Darker sediments signal dry/dusty conditions, lighter sediments signal

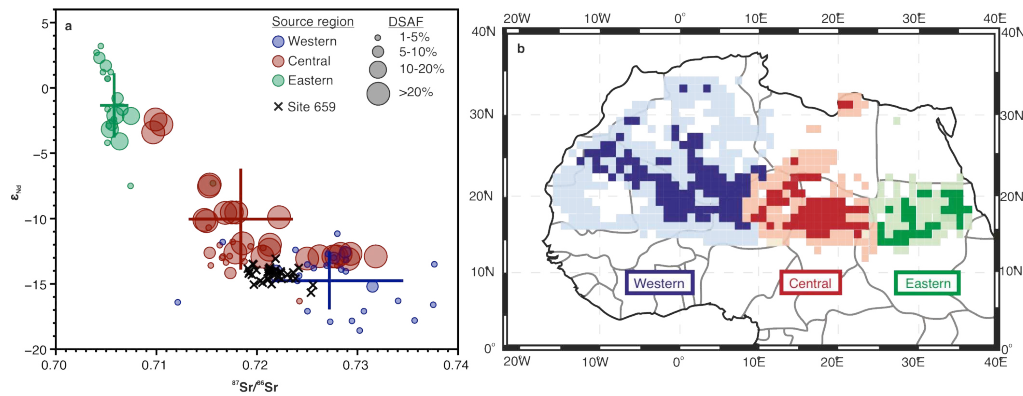
298

more humid intervals (see also Extended Data Figure 4 and Supplementary

299

Information).

300



302

303 **Figure 4| Radiogenic isotope signature of Site 659 lithic fraction compared to**304 **values of preferential source regions (PSAs) reveals consistent source. a** Site 659

305 bulk sediment data (black crosses) compared to source region measurements (circles)

306 coloured by PSA³¹. Data point size indicates dust source activation frequency307 (DSAF)²⁸. Crosses indicate mean signatures of each PSA weighted by annual DSAF,308 bars denote \pm one weighted standard deviation³¹. Samples for which only ϵ_{Nd} or309 $^{87}Sr/^{86}Sr$ data exist are included in the calculation of mean values but are not plotted.310 **b** Map of North African PSAs, adapted from ref. 31. Dust sources with activation

311 frequencies >5% shown in bold colours, <5% in pale colours.

312

313 **References**

- 314 1. Thomas N, Nigam S. Twentieth-Century Climate Change over Africa:
315 Seasonal Hydroclimate Trends and Sahara Desert Expansion. *Journal of*
316 *Climate* 2018, **31**(9): 3349-3370.
317
- 318 2. Maley J. Les changements climatiques de la fin du Tertiaire en Afrique: leur
319 conséquence sur l'apparition du Sahara et de sa végétation. *The Sahara and the*
320 *Nile* 1980: 63-86.
321
- 322 3. deMenocal PB. Plio-Pleistocene African Climate. *Science* 1995, **270**(5233):
323 53-59.

- 324
325 4. Trauth MH, Larrasoana JC, Mudelsee M. Trends, rhythms and events in Plio-
326 Pleistocene African climate. *Quaternary Science Reviews* 2009, **28**(5–6): 399-
327 411.
328
329 5. Muhs DR, Meco J, Budahn JR, Skipp GL, Betancort JF, Lomoschitz A. The
330 antiquity of the Sahara Desert: New evidence from the mineralogy and
331 geochemistry of Pliocene paleosols on the Canary Islands, Spain.
332 *Palaeogeography, Palaeoclimatology, Palaeoecology* 2019, **533**: 109245.
333
334 6. Schuster M, Durringer P, Ghienne J-F, Vignaud P, Mackaye HT, Likius A, *et*
335 *al.* The Age of the Sahara Desert. *Science* 2006, **311**(5762): 821.
336
337 7. Zhang Z, Ramstein G, Schuster M, Li C, Contoux C, Yan Q. Aridification of
338 the Sahara desert caused by Tethys Sea shrinkage during the Late Miocene.
339 *Nature* 2014, **513**(7518): 401-404.
340
341 8. Kroepelin S, Swezey CS. Revisiting the Age of the Sahara Desert. *Science*
342 2006, **312**(5777): 1138-1139.
343
344 9. McQuarrie N, van Hinsbergen DJJ. Retrodeforming the Arabia-Eurasia
345 collision zone: Age of collision versus magnitude of continental subduction.
346 *Geology* 2013, **41**(3): 315-318.
347
348 10. Allen MB, Armstrong HA. Arabia–Eurasia collision and the forcing of mid-
349 Cenozoic global cooling. *Palaeogeography, Palaeoclimatology,*
350 *Palaeoecology* 2008, **265**(1–2): 52-58.
351
352 11. Tiedemann R, Sarnthein M, Shackleton NJ. Astronomic timescale for the
353 Pliocene Atlantic $\delta^{18}\text{O}$ and dust flux records of Ocean Drilling Program Site
354 659. *Paleoceanography* 1994, **9**(4): 619-638.
355
356 12. Tjallingii R, Claussen M, Stuut J-BW, Fohlmeister J, Jahn A, Bickert T, *et al.*
357 Coherent high- and low-latitude control of the northwest African hydrological
358 balance. *Nature Geosci* 2008, **1**(10): 670-675.
359
360 13. Skonieczny C, Paillou P, Bory A, Bayon G, Biscara L, Crosta X, *et al.* African
361 humid periods triggered the reactivation of a large river system in Western
362 Sahara. *Nat Commun* 2015, **6**.
363
364 14. Ruddiman WF, Sarnthein M, Baldauf JG, *et al.* *Proc. ODP, Init. Repts., 108.*
365 College Station, TX (Ocean Drilling Program), 1989.
366
367 15. Skonieczny C, McGee D, Winckler G, Bory A, Bradtmiller LI, Kinsley CW,
368 *et al.* Monsoon-driven Saharan dust variability over the past 240,000 years.
369 *Science Advances* 2019, **5**(1): eaav1887.
370
371 16. McGee D, deMenocal PB, Winckler G, Stuut JBW, Bradtmiller LI. The
372 magnitude, timing and abruptness of changes in North African dust deposition

- 373 over the last 20,000 yr. *Earth and Planetary Science Letters* 2013, **371-372**:
374 163-176.
- 375
- 376 17. Mulitza S, Heslop D, Pittauerova D, Fischer HW, Meyer I, Stuut J-B, *et al.*
377 Increase in African dust flux at the onset of commercial agriculture in the
378 Sahel region. *Nature* 2010, **466**(7303): 226-228.
- 379
- 380 18. Drake NA, Blench RM, Armitage SJ, Bristow CS, White KH. Ancient
381 watercourses and biogeography of the Sahara explain the peopling of the
382 desert. *Proceedings of the National Academy of Sciences* 2011, **108**(2): 458-
383 462.
- 384
- 385 19. Larrasoana JC, Roberts AP, Rohling EJ. Dynamics of green Sahara periods
386 and their role in hominin evolution. *PloS one* 2013, **8**(10): e76514.
- 387
- 388 20. Tierney JE, Pausata FSR, deMenocal PB. Rainfall regimes of the Green
389 Sahara. *Science Advances* 2017, **3**(1).
- 390
- 391 21. Mori F. The earliest Saharan rock-engravings. *Antiquity* 1974, **48**(190): 87-92.
- 392
- 393 22. McGee D, Broecker WS, Winckler G. Gustiness: The driver of glacial
394 dustiness? *Quaternary Science Reviews* 2010, **29**(17-18): 2340-2350.
- 395
- 396 23. Herbert TD, Lawrence KT, Tzanova A, Peterson LC, Caballero-Gill R, Kelly
397 CS. Late Miocene global cooling and the rise of modern ecosystems. *Nature*
398 *Geosci* 2016, **9**(11): 843-847.
- 399
- 400 24. Abell JT, Winckler G, Anderson RF, Herbert TD. Poleward and weakened
401 westerlies during Pliocene warmth. *Nature* 2021, **589**(7840): 70-75.
- 402
- 403 25. Burls NJ, Fedorov AV. Wetter subtropics in a warmer world: Contrasting past
404 and future hydrological cycles. *Proceedings of the National Academy of*
405 *Sciences* 2017, **114**(49): 12888-12893.
- 406
- 407 26. Moussa A, Novello A, Lebatard A-E, Decarreau A, Fontaine C, Barboni D, *et*
408 *al.* Lake Chad sedimentation and environments during the late Miocene and
409 Pliocene: New evidence from mineralogy and chemistry of the Bol core
410 sediments. *Journal of African Earth Sciences* 2016, **118**: 192-204.
- 411
- 412 27. Washington R, Todd M, Middleton NJ, Goudie AS. Dust-Storm Source Areas
413 Determined by the Total Ozone Monitoring Spectrometer and Surface
414 Observations. *Annals of the Association of American Geographers* 2003,
415 **93**(2): 297-313.
- 416
- 417 28. Schepanski K, Tegen I, Macke A. Comparison of satellite based observations
418 of Saharan dust source areas. *Remote Sensing of Environment* 2012, **123**: 90-
419 97.
- 420

- 421 29. Westerhold T, Marwan N, Drury AJ, Liebrand D, Agnini C, Anagnostou E, *et al.* An astronomically dated record of Earth's climate and its predictability
422 over the last 66 million years. *Science* 2020, **369**(6509): 1383-1387.
423
424
- 425 30. Sarnthein M, Thiede J, Pflaumann U, Erlenkeuser H, Fütterer D, Koopmann
426 B, *et al.* Atmospheric and Oceanic Circulation Patterns off Northwest Africa
427 During the Past 25 Million Years. In: von Rad U, Hinz K, Sarnthein M,
428 Seibold E (eds). *Geology of the Northwest African Continental Margin*.
429 Springer Berlin Heidelberg: Berlin, Heidelberg, 1982, pp 545-604.
430
- 431 31. Jewell AM, Drake N, Crocker AJ, Bakker NL, Kunkelova T, Bristow CS, *et al.*
432 Three North African dust source areas and their geochemical fingerprint.
433 *Earth and Planetary Science Letters* 2021, **554**: 116645.
434
- 435 32. Cerling TE, Harris JM, MacFadden BJ, Leakey MG, Quade J, Eisenmann V,
436 *et al.* Global vegetation change through the Miocene/Pliocene boundary.
437 *Nature* 1997, **389**(6647): 153-158.
438
- 439 33. Feakins SJ, Levin NE, Liddy HM, Sieracki A, Eglinton TI, Bonnefille R.
440 Northeast African vegetation change over 12 m.y. *Geology* 2013, **41**(3): 295–
441 298.
442
- 443 34. Pagani M, Freeman KH, Arthur MA. Late Miocene Atmospheric CO₂
444 Concentrations and the Expansion of C₄ Grasses. *Science* 1999, **285**(5429):
445 876-879.
446
- 447 35. Beerling DJ, Osborne CP. The origin of the savanna biome. *Global Change*
448 *Biology* 2006, **12**(11): 2023-2031.
449
- 450 36. Polissar PJ, Rose C, Uno KT, Phelps SR, deMenocal P. Synchronous rise of
451 African C₄ ecosystems 10 million years ago in the absence of aridification.
452 *Nature Geoscience* 2019, **12**(8): 657-660.
453
- 454 37. Hoetzel S, Dupont L, Schefuß E, Rommerskirchen F, Wefer G. The role of
455 fire in Miocene to Pliocene C₄ grassland and ecosystem evolution. *Nature*
456 *Geosci* 2013, **6**(12): 1027-1030.
457
- 458 38. Naafs BDA, Hefter J, Acton G, Haug GH, Martínez-García A, Pancost R, *et al.*
459 Strengthening of North American dust sources during the late Pliocene (2.7
460 Ma). *Earth and Planetary Science Letters* 2012, **317–318**(0): 8-19.
461
- 462 39. Kuechler RR, Dupont LM, Schefuß E. Hybrid insolation forcing of Pliocene
463 monsoon dynamics in West Africa. *Climate of the Past* 2018, **14**(1): 73-84.
464
- 465 40. Kuechler RR, Schefuß E, Beckmann B, Dupont L, Wefer G. NW African
466 hydrology and vegetation during the Last Glacial cycle reflected in plant-wax-
467 specific hydrogen and carbon isotopes. *Quaternary Science Reviews* 2013,
468 **82**(0): 56-67.
469

- 470 41. Cerling TE, Wynn JG, Andanje SA, Bird MI, Korir DK, Levin NE, *et al.*
471 Woody cover and hominin environments in the past 6 million years. *Nature*
472 2011, **476**(7358): 51-56.
473
- 474 42. Faith JT, Rowan J, Du A, Koch PL. Plio-Pleistocene decline of African
475 megaherbivores: No evidence for ancient hominin impacts. *Science* 2018,
476 **362**(6417): 938-941.
477
- 478 43. Potts R. Hominin evolution in settings of strong environmental variability.
479 *Quaternary Science Reviews* 2013, **73**: 1-13.
480
- 481 44. Maslin MA, Brierley CM, Milner AM, Shultz S, Trauth MH, Wilson KE. East
482 African climate pulses and early human evolution. *Quaternary Science*
483 *Reviews* 2014, **101**(0): 1-17.
484
- 485 45. Zollikofer CPE, Ponce de León MS, Lieberman DE, Guy F, Pilbeam D, Likius
486 A, *et al.* Virtual cranial reconstruction of Sahelanthropus tchadensis. *Nature*
487 2005, **434**: 755.
488
- 489 46. DiMaggio EN, Campisano CJ, Rowan J, Dupont-Nivet G, Deino AL, Bibi F,
490 *et al.* Late Pliocene fossiliferous sedimentary record and the environmental
491 context of early *Homo* from Afar, Ethiopia. *Science* 2015, **347**(6228): 1355-
492 1359.
493
- 494 47. Bobe R, Wood B. Estimating origination times from the early hominin fossil
495 record. *Evolutionary Anthropology: Issues, News, and Reviews* 2021: 1– 11.
496
- 497 48. Uno KT, Polissar PJ, Jackson KE, deMenocal PB. Neogene biomarker record
498 of vegetation change in eastern Africa. *Proceedings of the National Academy*
499 *of Sciences* 2016: 201521267.
500
- 501 49. Laskar J, Robutel P, Joutel F, Gastineau M, Correia ACM, Levrard B. A long-
502 term numerical solution for the insolation quantities of the Earth. *Astronomy &*
503 *Astrophysics* 2004, **428**(1): 261-285.
504

505 **Methods**

506 **Site Location**

507 ODP Site 659 is situated in the tropical North Atlantic Ocean on the Cape Verde Rise,
508 offshore Mauritania (18.077°N 21.026°W, 3070 m water depth, for map see
509 Supplementary Figure 1). Today, this region receives dust delivered by the trade
510 winds during winter and spring, with additional dust transported over the site by the
511 Saharan Air Layer predominantly during boreal summer⁵⁰⁻⁵⁶. The Algeria-Morocco
512 region, Mali, Mauritania, Libya, Niger, Western Sahara and the Sahel have all been
513 identified as regions that may currently contribute dust to the Cape Verde Islands and
514 the surrounding ocean sediments, while evidence for a major contribution from the
515 Bodélé depression is weaker^{50-53,56-65}. The elevated position of Site 659 on the Cape
516 Verde Rise protects it from major mass transport deposits, although grain size data
517 reveal that multiple sites along the northwestern African margin including
518 GeoB7920¹² and Site 659 received a significant fine-grained lithogenic component
519 during both the Holocene and last glacial cycle that is distinct from modern dust
520 inputs and is often attributed to a distal influence from African (palaeo)rivers¹²
521 (Extended Data Figures 9–10 and Supplementary Information).

522

523 **X-ray fluorescence**

524 Data were collected from a total of about 275 m of drill core from three holes at ODP
525 Site 659 using the XRF Core Scanner II (AVAATECH Serial No. 2) at MARUM -
526 University of Bremen. Measurements were taken every 1–5 cm down core to give a
527 consistent approximate temporal resolution of 1.5–2 kyr. Count times were 20
528 seconds and generator settings of 30 and 10 kV with currents of 0.75 and 0.2 mA
529 respectively were used. The split core surface was covered with a 4 micron thin

530 SPEXCerti Prep Ultralene foil to avoid contamination of the XRF measurement unit
531 and desiccation of the sediment. The data were acquired using a Canberra X-PIPS
532 Silicon Drift Detector (SDD; Model SXD 15C-150-500) with 150eV X-ray
533 resolution, the Canberra Digital Spectrum Analyzer DAS 1000, and an Oxford
534 Instruments 50W XTF5011 X-Ray tube with rhodium (Rh) target material. Raw X-
535 ray spectra were processed using an iterative least square software (WIN AXIL)
536 package from Canberra Eurisys. Repeat runs of several core sections were used to
537 correct for any drift in counts over time.

538

539 Ca/Fe ratios provide an indicator of the relative proportions of marine (dominated by
540 biogenic calcium carbonate) and terrigenous (the main source of iron) sediment
541 (Supplementary Figure 4). We use two geochemical ratios to determine the relative
542 contribution of aeolian material to the sediment. Modern Saharan dust has much
543 lower $[Al+Fe]/[Si+K+Ti]$ values than samples of suspended sediment from the
544 Senegal River (Figure 1f), the nearest and largest active river to Site 659, which
545 drains deeply weathered lateritic tropical soils much richer in Al and Fe than the Si-
546 rich Sahelian/Saharan dust sources¹⁷. We also employ Zr/Rb as an independent grain
547 size proxy because the lithogenic dust fraction is significantly coarser than riverine-
548 derived material on the northwest African margin^{12,66}, and contains a higher
549 proportion of Zr-bearing zircon grains than Rb-rich river clays⁶⁷. Additional
550 geochemical ratios are shown in Supplementary Figures 5–6. Our XRF records have
551 an average temporal resolution of approximately 2000 years.

552

553 A suite of discrete sediment samples from ODP Site 659 incorporating a wide range
554 of lithologies were analysed by energy dispersive polarised x-ray fluorescence

555 spectrometry (EDP-XRF) at the University of St Andrews to convert the semi-
556 quantitative XRF scanner counts into concentrations (Supplementary Figure 7). The
557 downcore records plotted are calculated from ratios of these calibrated values, except
558 for $\ln[\text{Zr/Rb}]$ where counts of these trace elements are plotted.

559

560 **Stratigraphy**

561 We created a new spliced composite section for ODP Site 659 to a depth of 203.17
562 revised metres composite depth (rmcd) by correlating both the XRF core scan data
563 and core images between the three holes (A–C) drilled at Site 659, using the Code for
564 Ocean Drilling Data macros⁶⁸. An age framework was developed from paleomagnetic,
565 nannofossil and planktonic foraminiferal datums^{14,69} with ages updated to incorporate
566 more recent improvements in astrochronology⁷⁰⁻⁷². We then correlated previously
567 published oxygen isotope values of the benthic foraminifera *Cibicides wuellerstorfi* at
568 Site 659¹¹ transferred onto our composite depth scale to the LR04 benthic oxygen
569 isotope stack⁷³ to improve age control for the youngest 5 Myr. The final age model
570 was then generating by tuning our XRF count data ($\ln[\text{Ca/Fe}]$) to summer insolation
571 calculated at 65°N in the La2004 astronomical solution⁴⁹, guided by the framework
572 provided by the biostratigraphic, magnetostratigraphic and benthic oxygen isotope
573 record. The construction of this age model is illustrated in Supplementary Figure 8. In
574 Supplementary Figure 2, we compare the age-depth relationship of our
575 astronomically-tuned age model to existing bio- and magnetostratigraphic datums.
576 Continuous wavelet power spectra⁷⁴ of both astronomically-tuned and non-
577 astronomically tuned time series data are shown in Extended Data Figure 5, with
578 results from REDFIT⁷⁵ spectral analysis shown in Extended Data Figure 6.

579

580 **Geochemical end-member unmixing**

581 Dust fluxes were estimated using an end-member unmixing approach to deconvolve
582 the relative proportions of different contributions to the bulk marine sediment, largely
583 following the method of Mulitza et al. (2010)¹⁷. In this approach, bulk sediment is
584 assumed to consist of three components: aeolian, riverine and marine inputs. The
585 relative abundances of Al, Si, Fe, K, Ti and Ca concentrations at Site 659 (calibrated
586 by a multivariate log calibration method^{76,77} using the AvaaXelerate software⁷⁸) were
587 compared to the chemistry of endmember compositions estimated from analyses of
588 modern sediments. The riverine endmember was constructed from ten measurements
589 of suspended sediment from the Senegal River⁷⁹, the present day catchment of which
590 stretches both north and south of Site 659. A total of 48 measurements were used to
591 construct a dust endmember, covering a wide geographical area and incorporating
592 data from dust traps, atmospheric sampling and bulk sediment from known dust
593 source areas with a range of grain sizes and local climates^{59,62,80-91}. A marine
594 endmember composition of 2% Si and 98% Ca was assumed¹⁷. To incorporate the
595 effect of temporal changes in active terrigenous source regions and lithic fraction
596 chemistry into our dust flux estimates, a bootstrapping approach was applied. During
597 every realization, 10 of the 48 dust compositions and 4 of the 10 river compositions
598 were selected by a bootstrap with replacement routine, with the unmixing procedure
599 carried out for a total of 500 realizations of endmember compositions. Proportions of
600 aeolian and riverine endmembers were converted to fluxes using sedimentation rates
601 calculated from our composite depth scale and age model, and dry bulk sediment
602 densities estimated from shipboard measurements of gamma-ray attenuation¹⁴ which
603 were calibrated using the discrete dry bulk density measurements of Tiedemann
604 (1991)⁹². We show that there is good agreement between our dust flux estimates and

605 those based on ^{230}Th normalization¹⁵ and lithogenic %¹¹ in Extended Data Figures 2–
606 3, Supplementary Figure 4 and Supplementary Information.

607

608 Lithogenic grain size measurements and geochemical data strongly support the
609 concept of distal riverine inputs to Site 659. The proportion of the terrigenous fraction
610 that is attributed to aeolian inputs by this geochemical unmixing approach varies
611 strongly down core, with estimates of 0–87% dust origin. These estimates are broadly
612 in line with those of Tjallingii et al. (2008)¹² who find that dust accounts for 5–95% of
613 the lithic fraction through the last glacial cycle at nearby site GeoB7920 using a
614 unmixing approach based upon grain size distributions. We cannot, however, rule out
615 contributions to the fine-grained, high Al+Fe end-member from very fine dust or
616 resuspended shelf material. Thus, our dust fluxes are minimum (conservative)
617 estimates (see Supplementary Information).

618

619 **Radiogenic isotopes**

620 The Sr and Nd isotope composition of terrigenous sediments from ODP Site 659 were
621 measured at the University of Southampton National Oceanography Centre.

622 Approximately 1g of crushed and homogenised dried bulk sediment was decarbonated
623 using 10 % acetic acid solution for 24 hours on a shaker table and then rinsed in
624 deionized water. Samples were placed in a 5 % hydrogen peroxide solution for 48
625 hours at 65 °C to remove organic matter, then rinsed three times in deionized water.
626 1M MgCl_2 was added to the samples to remove any Sr adsorbed from seawater, which
627 were shaken overnight then rinsed three times. A buffered hydroxylamine HCl, Na-
628 EDTA and acetic acid solution was added to remove authigenic coatings, with
629 samples mixed for 24 hours and then rinsed. A magnesium ion solution was added to

630 aid flocculation if a colloid phase formed at any stage during processing. The
631 'cleaned' sediments were then totally digested in concentrated nitric acid (HNO₃) and
632 hydrofluoric acid (HF), followed by 6M HCl.

633

634 Digested sediment solutions for Sr isotope analysis were purified on columns filled
635 with Sr-spec Resin in 3M HNO₃. Samples were loaded onto tantalum (Ta) filaments
636 with a 1M HCl solution after a tantalum chloride (TaCl) activator solution was
637 loaded. Isotopic measurements were made by thermal ionization mass spectrometry
638 (Thermo-Fisher TRITON Plus). Repeated measurements of the Sr isotope standard
639 NBS987 gave $^{87}\text{Sr}/^{86}\text{Sr} = 0.710243 \pm 0.000021$ (2σ).

640

641 Neodymium was purified from the digested sediments for isotope analysis using a
642 standard column chemistry procedure, based upon the methods of Cohen et al.
643 (1988)⁹³. Cation exchange resin was used to strip iron and titanium from the samples,
644 then the remaining material was then run through using Ln-SpecTM resin columns⁹⁴ to
645 purify and concentrate neodymium. Neodymium isotope ratios were measured by
646 multi-collector inductively coupled plasma mass spectrometry (Thermo NEPTUNE).
647 Instrumental mass bias was corrected using the procedure of Vance and Thirlwall
648 (2002)⁹⁵, adjusting to a $^{146}\text{Nd}/^{144}\text{Nd}$ ratio of 0.7219 and using cerium-doped standards
649 to correct for interference of ^{142}Ce on ^{142}Nd . All ratios were normalised to the JNdi-1
650 standard ($^{143}\text{Nd}/^{144}\text{Nd} = 0.512115 \pm 0.000007$)⁹⁶, with independent measurements of
651 JNdi-1 = 0.512115 ± 0.000006 (2σ). Isotopic signatures are expressed in epsilon
652 notation, relative to the chondritic uniform reservoir value of 0.512638⁹⁷.

653

654 **Leaf wax $\delta^{13}\text{C}$**

655 Compound specific stable carbon isotopes ($\delta^{13}\text{C}$) of the C_{31} and C_{33} *n*-alkane were
656 obtained from 30 samples from ODP Site 659 at the Organic Geochemistry Unit,
657 University of Bristol. For this purpose, between 5 and 10 gram of freeze-dried
658 sediment was extracted using a Microwave extraction system (Milestone Ethos Ex)
659 and a mixture of dichloromethane (DCM) and methanol (MeOH) (9:1, v/v). Fine
660 grained sediment was removed by eluting the total lipid extract (TLE) over a short (4
661 cm) inert NaSO_4 column using 4 ml of DCM:MeOH (9:1). The TLE was dried under
662 a gentle flow of N_2 . The TLE was subsequently derivatized using pyridine and
663 BSFTA (1 hr at 70 °C) and within 24 hrs analysed on an Isoprime 100 gas
664 chromatograph combustion isotope ratio mass spectrometer (GC-C-IRMS). Samples
665 were measured in triplicate and $\delta^{13}\text{C}$ values converted to VPDB by bracketing with an
666 in-house gas (CO_2) of known $\delta^{13}\text{C}$ value. Instrument stability was monitored by
667 regular analysis of an in-house fatty acid methyl ester standard mixture and indicates
668 that long-term instrument stability was better than ± 0.3 ‰. Injection volume was 1
669 or 2 μl onto to a Zebron-I nonpolar column (50 m x 0.32 mm i.d., 0.10 μm film
670 thickness). The GC oven was programmed as: 70 °C (1 min hold) to 130 °C at 20 °C
671 min^{-1} , then to 300 °C at 4 °C min^{-1} , and a final hold at 300 °C for 25 min. Samples
672 were automatically integrated using the Ion Vantage software.

673

674 For some samples, the concentration of the C_{33} *n*-alkane was not enough to obtain a
675 reliable $\delta^{13}\text{C}$ value. The $\delta^{13}\text{C}$ of the C_{31} *n*-alkane was consistently lighter than that of
676 the C_{33} *n*-alkane from the same sample by on average 2 ‰.

677

678 **Lithogenic grain size distributions at ODP Site 659**

679 The distribution of grain sizes in lithogenic material can be used to identify different
680 terrigenous components in marine sediment. 55 samples from ODP Site 659 were
681 selected to generate grain size distribution data, incorporating a range of sediment
682 ages and lithologies. Calcium carbonate, authigenic coatings and organic matter were
683 removed following the procedure used for radiogenic isotope analysis. In addition, a
684 biogenic silica removal step was applied by sonicating samples in 1.5M NaOH.
685 Calgon was then added to the samples to prevent flocculation before analysis of the
686 lithogenic grain sizes using a Laser Coulter Sizer at the University of Southampton
687 Waterfront Campus, NOCS. The results of these grain size analyses are shown in
688 Extended Data Figure 9d.

689

690 The signatures of different terrigenous sources were separated from the bulk sediment
691 signature following the end-member modeling analysis approach (EMMA) of Dietze
692 et al. (2011)⁹⁸. A two lithogenic end-member solution explains 88% of the variance in
693 the Site 659 data set, with the end-members shown in Extended Figure 9. The coarser
694 of these two endmembers shows a strong match with measurements of African dust
695 (Extended Data Figure 9a-b)

696

697 **Data availability**

698 The data presented in this study are available in the Zenodo repository (DOI:
699 10.5281/zenodo.6594643).

700

701 **Methods references**

702

703 50. Kumar A, Abouchami W, Galer SJG, Singh SP, Fomba KW, Prospero JM, *et*
704 *al.* Seasonal radiogenic isotopic variability of the African dust outflow to the

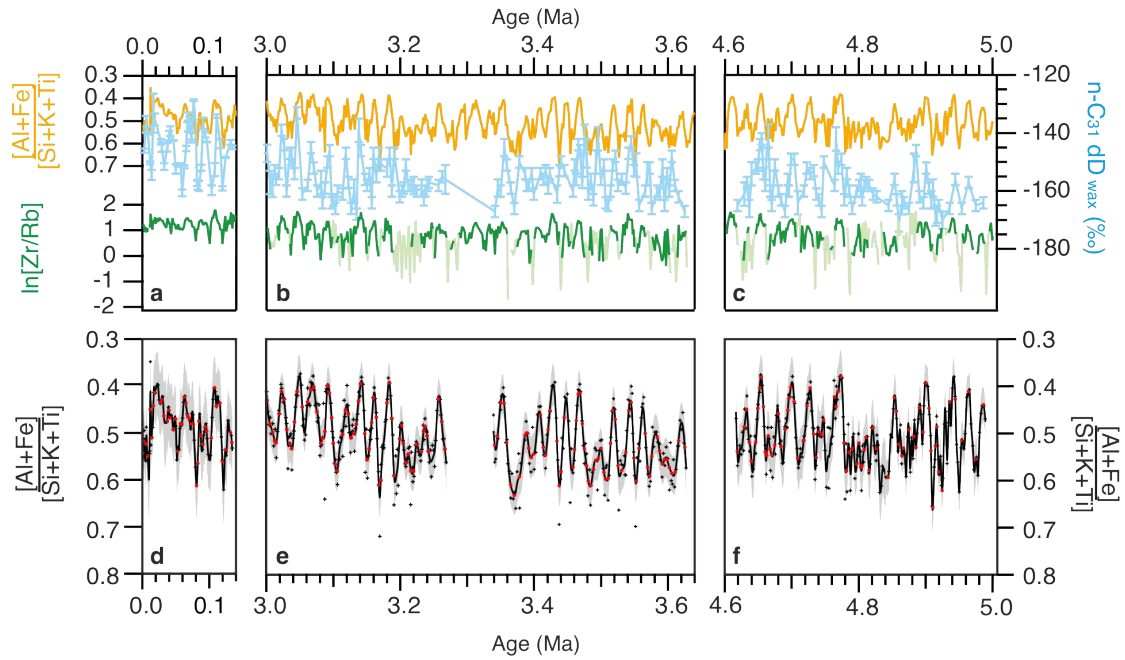
- 705 tropical Atlantic Ocean and across to the Caribbean. *Earth and Planetary*
706 *Science Letters* 2018, **487**: 94-105.
- 707
- 708 51. Gama C, Tchepel O, Baldasano JM, Basart S, Ferreira J, Pio C, *et al.* Seasonal
709 patterns of Saharan dust over Cape Verde – a combined approach using
710 observations and modelling. *Tellus B: Chemical and Physical Meteorology*
711 2015, **67**(1): 24410.
- 712
- 713 52. Patey MD, Achterberg EP, Rijkenberg MJ, Pearce R. Aerosol time-series
714 measurements over the tropical Northeast Atlantic Ocean: Dust sources,
715 elemental composition and mineralogy. *Marine Chemistry* 2015, **174**: 103-
716 119.
- 717
- 718 53. Skonieczny C, Bory A, Bout-Roumazielles V, Abouchami W, Galer SJG,
719 Crosta X, *et al.* A three-year time series of mineral dust deposits on the West
720 African margin: Sedimentological and geochemical signatures and
721 implications for interpretation of marine paleo-dust records. *Earth and*
722 *Planetary Science Letters* 2013, **364**: 145-156.
- 723
- 724 54. Ratmeyer V, Fischer G, Wefer G. Lithogenic particle fluxes and grain size
725 distributions in the deep ocean off northwest Africa: Implications for seasonal
726 changes of aeolian dust input and downward transport. *Deep Sea Research*
727 *Part I: Oceanographic Research Papers* 1999, **46**(8): 1289-1337.
- 728
- 729 55. Bory A, Dulac F, Moulin C, Chiapello I, Newton PP, Guelle W, *et al.*
730 Atmospheric and oceanic dust fluxes in the northeastern tropical Atlantic
731 Ocean: how close a coupling? *Ann Geophys* 2002, **20**(12): 2067-2076.
- 732
- 733 56. Chiapello I, Bergametti G, Chatenet B, Bousquet P, Dulac F, Soares ES.
734 Origins of African dust transported over the northeastern tropical Atlantic.
735 *Journal of Geophysical Research: Atmospheres* 1997, **102**(D12): 13701-
736 13709.
- 737
- 738 57. Schepanski K, Tegen I, Macke A. Saharan dust transport and deposition
739 towards the tropical northern Atlantic. *Atmos Chem Phys* 2009, **9**(4): 1173-
740 1189.
- 741
- 742 58. Caquineau S, Gaudichet A, Gomes L, Legrand M. Mineralogy of Saharan dust
743 transported over northwestern tropical Atlantic Ocean in relation to source
744 regions. *Journal of Geophysical Research: Atmospheres* 2002, **107**(D15):
745 AAC 4-1-AAC 4-12.
- 746
- 747 59. Formenti P, Rajot JL, Desboeufs K, Caquineau S, Chevaillier S, Nava S, *et al.*
748 Regional variability of the composition of mineral dust from western Africa:
749 Results from the AMMA SOP0/DABEX and DODO field campaigns. *Journal*
750 *of Geophysical Research: Atmospheres* 2008, **113**(D23): D00C13.
- 751
- 752 60. Friese CA, van Hateren JA, Vogt C, Fischer G, Stuut J-BW. Seasonal
753 provenance changes in present-day Saharan dust collected in and off
754 Mauritania. *Atmospheric Chemistry and Physics* 2017, **17**(16): 10163.

- 755
756 61. McConnell CL, Highwood EJ, Coe H, Formenti P, Anderson B, Osborne S, *et al.* Seasonal variations of the physical and optical characteristics of Saharan
757 dust: Results from the Dust Outflow and Deposition to the Ocean (DODO)
758 experiment. *Journal of Geophysical Research: Atmospheres* 2008, **113**(D14).
759
760
761 62. Salvador P, Almeida SM, Cardoso J, Almeida-Silva M, Nunes T, Cerqueira
762 M, *et al.* Composition and origin of PM10 in Cape Verde: Characterization of
763 long-range transport episodes. *Atmospheric Environment* 2016, **127**: 326-339.
764
765 63. Skonieczny C, Bory A, Bout-Roumazeilles V, Abouchami W, Galer SJG,
766 Crosta X, *et al.* The 7–13 March 2006 major Saharan outbreak: Multiproxy
767 characterization of mineral dust deposited on the West African margin.
768 *Journal of Geophysical Research: Atmospheres* 2011, **116**(D18).
769
770 64. Stuut J-B, Zabel M, Rattmeyer V, Helmke P, Schefuß E, Lavik G, *et al.*
771 Provenance of present-day eolian dust collected off NW Africa. *Journal of*
772 *Geophysical Research: Atmospheres* 2005, **110**(D4): D04202.
773
774 65. Zhao W, Balsam W, Williams E, Long X, Ji J. Sr–Nd–Hf isotopic
775 fingerprinting of transatlantic dust derived from North Africa. *Earth and*
776 *Planetary Science Letters* 2018, **486**: 23-31.
777
778 66. Holz C, Stuut J-BW, Henrich R. Terrigenous sedimentation processes along
779 the continental margin off NW Africa: implications from grain-size analysis of
780 seabed sediments. *Sedimentology* 2004, **51**(5): 1145-1154.
781
782 67. Matthewson AP, Shimmield GB, Kroon D, Fallick AE. A 300 kyr high-
783 resolution aridity record of the North African continent. *Paleoceanography*
784 1995, **10**(3): 677-692.
785
786 68. Wilkens RH, Westerhold T, Drury AJ, Lyle M, Gorgas T, Tian J. Revisiting
787 the Ceara Rise, equatorial Atlantic Ocean: isotope stratigraphy of ODP Leg
788 154 from 0 to 5 Ma. *Clim Past* 2017, **13**(7): 779-793.
789
790 69. Manivit H. Calcareous nannofossil biostratigraphy of Leg 108 sediments. In:
791 Ruddiman W, Sarnthein, M., *et al.*, (ed). *Proceedings of the Ocean Drilling*
792 *Program, Scientific Results, Vol.108*, 1989, pp 35-69.
793
794 70. Raffi I, Backman J, Fornaciari E, Pälike H, Rio D, Lourens L, *et al.* A review
795 of calcareous nannofossil astrobiochronology encompassing the past 25
796 million years. *Quaternary Science Reviews* 2006, **25**(23–24): 3113-3137.
797
798 71. Ogg JG. Chapter 5 - Geomagnetic Polarity Time Scale. In: Gradstein FM, Ogg
799 JG, Schmitz MD, Ogg GM (eds). *The Geologic Time Scale*. Elsevier: Boston,
800 2012, pp 85-113.
801
802 72. Wade BS, Pearson PN, Berggren WA, Pälike H. Review and revision of
803 Cenozoic tropical planktonic foraminiferal biostratigraphy and calibration to

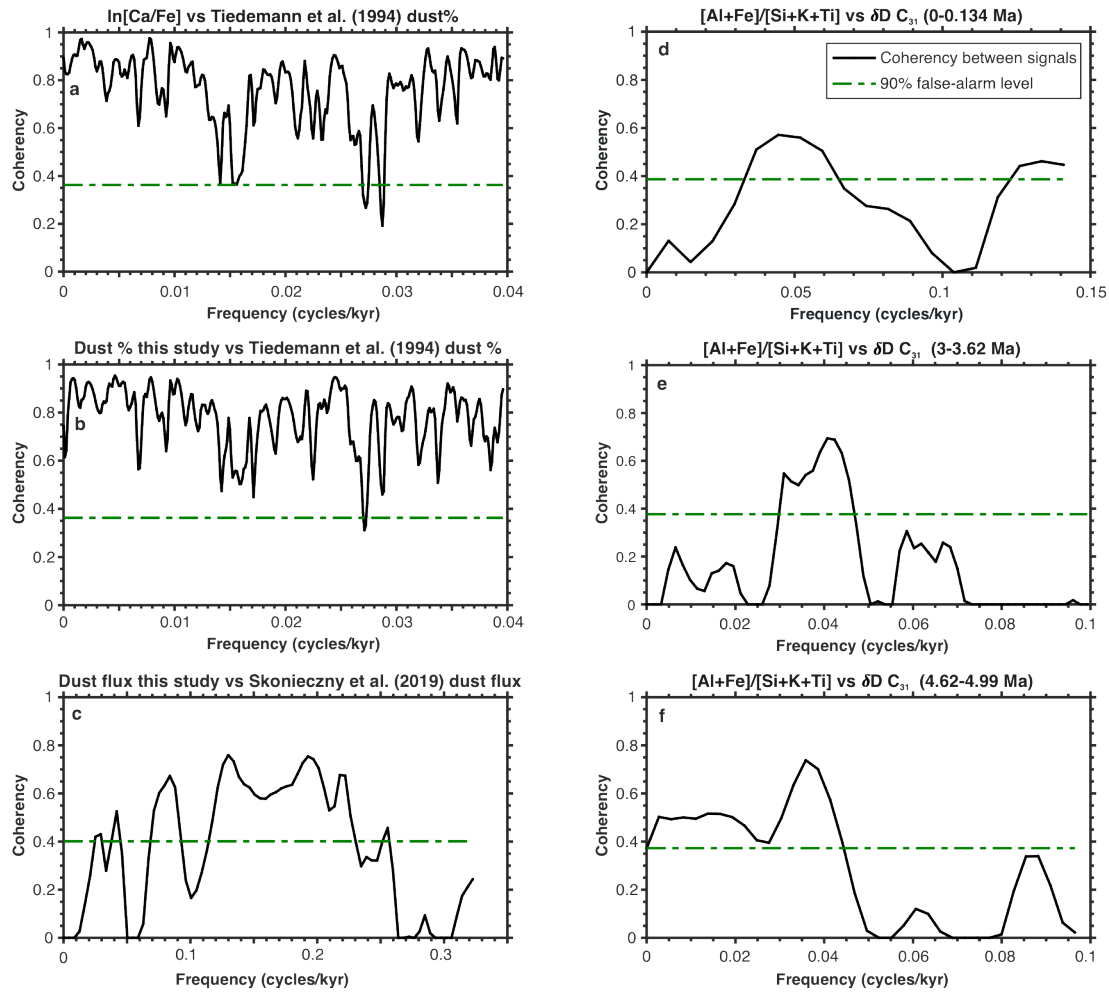
- 804 the geomagnetic polarity and astronomical time scale. *Earth-Science Reviews*
805 2011, **104**(1): 111-142.
- 806
- 807 73. Lisiecki LE, Raymo ME. A Pliocene-Pleistocene stack of 57 globally
808 distributed benthic $\delta^{18}\text{O}$ records. *Paleoceanography* 2005, **20**(1).
- 809
- 810 74. Grinsted A, Moore JC, Jevrejeva S. Application of the cross wavelet transform
811 and wavelet coherence to geophysical time series. *Nonlinear processes in*
812 *geophysics* 2004, **11**(5/6): 561-566.
- 813
- 814 75. Schulz M, Mudelsee M. REDFIT: estimating red-noise spectra directly from
815 unevenly spaced paleoclimatic time series. *Computers & Geosciences* 2002,
816 **28**(3): 421-426.
- 817
- 818 76. Weltje GJ, Tjallingii R. Calibration of XRF core scanners for quantitative
819 geochemical logging of sediment cores: Theory and application. *Earth and*
820 *Planetary Science Letters* 2008, **274**(3-4): 423-438.
- 821
- 822 77. Weltje GJ, Bloemsa M, Tjallingii R, Heslop D, Röhl U, Croudace IW.
823 Prediction of geochemical composition from XRF core scanner data: a new
824 multivariate approach including automatic selection of calibration samples and
825 quantification of uncertainties. In: Croudace; IW, Rothwell RG (eds). *Micro-*
826 *XRF Studies of Sediment Cores*. Springer, 2015, pp 507-534.
- 827
- 828 78. Bloemsa MR. Development of a Modelling Framework for Core Data
829 Integration using XRF Scanning. TU Delft, Delft University of Technology,
830 2015.
- 831
- 832 79. Gac J-Y, Kane A. Le fleuve Sénégal: I. Bilan hydrologique et flux
833 continentaux de matières particulaires à l'embouchure. *Sciences Géologiques,*
834 *bulletins et mémoires* 1986: 99-130.
- 835
- 836 80. Scheuven D, Schütz L, Kandler K, Ebert M, Weinbruch S. Bulk composition
837 of northern African dust and its source sediments — A compilation. *Earth-*
838 *Science Reviews* 2013, **116**(0): 170-194.
- 839
- 840 81. Orange D, Gac J-Y. Bilan géochimique des apports atmosphériques en
841 domaines sahélien et soudano-guinéen d'Afrique de l'Ouest (bassins supérieurs
842 du Sénégal et de la Gambie). *Géodynamique* 1990, **5**(1): 51-65.
- 843
- 844 82. Orange D, Gac J-Y, Diallo MI. Geochemical assessment of atmospheric
845 deposition including Harmattan dust in continental West Africa. Tracers in
846 Hydrology; 1993: IAHS; 1993.
- 847
- 848 83. Guieu C, Thomas AJ. Saharan Aerosols: From the Soil to the Ocean. In:
849 Guerzoni S, Chester R (eds). *The Impact of Desert Dust Across the*
850 *Mediterranean*. Springer Netherlands: Dordrecht, 1996, pp 207-216.
- 851

- 852 84. Criado C, Dorta P. An unusual ‘blood rain’ over the Canary Islands (Spain).
853 The storm of January 1999. *Journal of Arid Environments* 2003, **55**(4): 765-
854 783.
- 855
- 856 85. Viana M, Querol X, Alastuey A, Cuevas E, Rodríguez S. Influence of African
857 dust on the levels of atmospheric particulates in the Canary Islands air quality
858 network. *Atmospheric Environment* 2002, **36**(38): 5861-5875.
- 859
- 860 86. Formenti P, Elbert W, Maenhaut W, Haywood J, Andreae MO. Chemical
861 composition of mineral dust aerosol during the Saharan Dust Experiment
862 (SHADE) airborne campaign in the Cape Verde region, September 2000.
863 *Journal of Geophysical Research: Atmospheres* 2003, **108**(D18): 8576.
- 864
- 865 87. Linke C, Möhler O, Veres A, Mohácsi Á, Bozóki Z, Szabó G, *et al.* Optical
866 properties and mineralogical composition of different Saharan mineral dust
867 samples: a laboratory study. *Atmospheric Chemistry and Physics* 2006, **6**(11):
868 3315-3323.
- 869
- 870 88. Khiri F, Ezaidi A, Kabbachi K. Dust deposits in Souss–Massa basin, South-
871 West of Morocco: granulometrical, mineralogical and geochemical
872 characterisation. *Journal of African Earth Sciences* 2004, **39**(3): 459-464.
- 873
- 874 89. Moreno T, Querol X, Castillo S, Alastuey A, Cuevas E, Herrmann L, *et al.*
875 Geochemical variations in aeolian mineral particles from the Sahara–Sahel
876 Dust Corridor. *Chemosphere* 2006, **65**(2): 261-270.
- 877
- 878 90. Mounkaila M. Spectral and Mineralogical Properties of Potential Dust Sources
879 on a Transect from the Bodélé Depresseion (Central Sahara) to the Lake Chad
880 in the Sahel. *Hohenheimer Bodenkundliche Hefte* 2006, **78**: 1-311.
- 881
- 882 91. Herrmann L, Jahn R, Maurer T. Mineral dust around the Sahara—from source
883 to sink. A review with emphasis on contributions of the German soil science
884 community in the last twenty years. *Journal of Plant Nutrition and Soil
885 Science* 2010, **173**(6): 811-821.
- 886
- 887 92. Tiedemann R. Acht Millionen Jahre Klimageschichte von Nordwest Afrika
888 und Paläo-Ozeanographie des angrenzenden Atlantiks: Hochauflösende
889 Zeitreihen von ODP-Sites 658-661. Christian-Albrechts-Universität, 1991.
- 890
- 891 93. Cohen AS, O’Nions RK, Siegenthaler R, Griffin WL. Chronology of the
892 pressure-temperature history recorded by a granulite terrain. *Contributions to
893 Mineralogy and Petrology* 1988, **98**(3): 303-311.
- 894
- 895 94. Pin C, Zalduegui JS. Sequential separation of light rare-earth elements,
896 thorium and uranium by miniaturized extraction chromatography: Application
897 to isotopic analyses of silicate rocks. *Analytica Chimica Acta* 1997, **339**(1–2):
898 79-89.
- 899
- 900 95. Vance D, Archer C. Isotopic constraints on the origin of Heinrich event
901 precursors. *Goldschmidt Conference Abstract*, 2002.

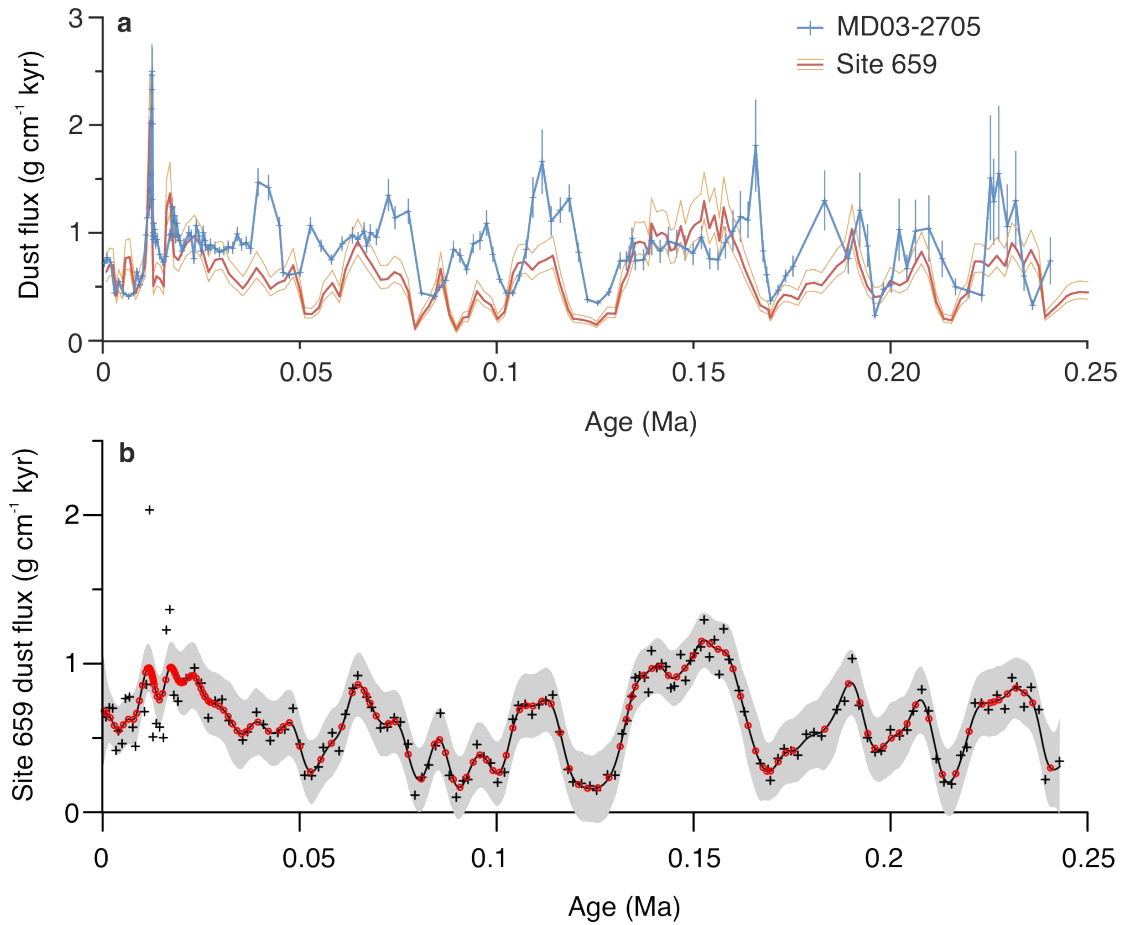
- 902
903 96. Tanaka T, Togashi S, Kamioka H, Amakawa H, Kagami H, Hamamoto T, *et*
904 *al.* JNdi-1: a neodymium isotopic reference in consistency with LaJolla
905 neodymium. *Chemical Geology* 2000, **168**(3–4): 279-281.
906
907 97. Jacobsen SB, Wasserburg GJ. Sm-Nd isotopic evolution of chondrites. *Earth*
908 *and Planetary Science Letters* 1980, **50**(1): 139-155.
909
910 98. Dietze, E. *et al.* An end-member algorithm for deciphering modern detrital
911 processes from lake sediments of Lake Donggi Cona, NE Tibetan Plateau,
912 China. *Sedimentary Geology* **243-244**, 169-180 (2011).
913
914 99. Wood, S. N. *Generalized additive models: an introduction with R.* (CRC
915 press, 2017).
916
917 100. Grinsted, A., Moore, J. C. & Jevrejeva, S. Application of the cross wavelet
918 transform and wavelet coherence to geophysical time series. *Nonlinear*
919 *processes in geophysics* **11**, 561-566 (2004).
920
921 101. Hammer, Ø., Harper, D. A. T. & Ryan, P. D. PAST: Paleontological Statistics
922 Software Package for Education and Data Analysis. *Palaeontologia*
923 *Electronica* **4**, 9 (2001).
924
925 102. Castillo, S. *et al.* Trace element variation in size-fractionated African desert
926 dusts. *Journal of Arid Environments* **72**, 1034-1045 (2008).
927
928



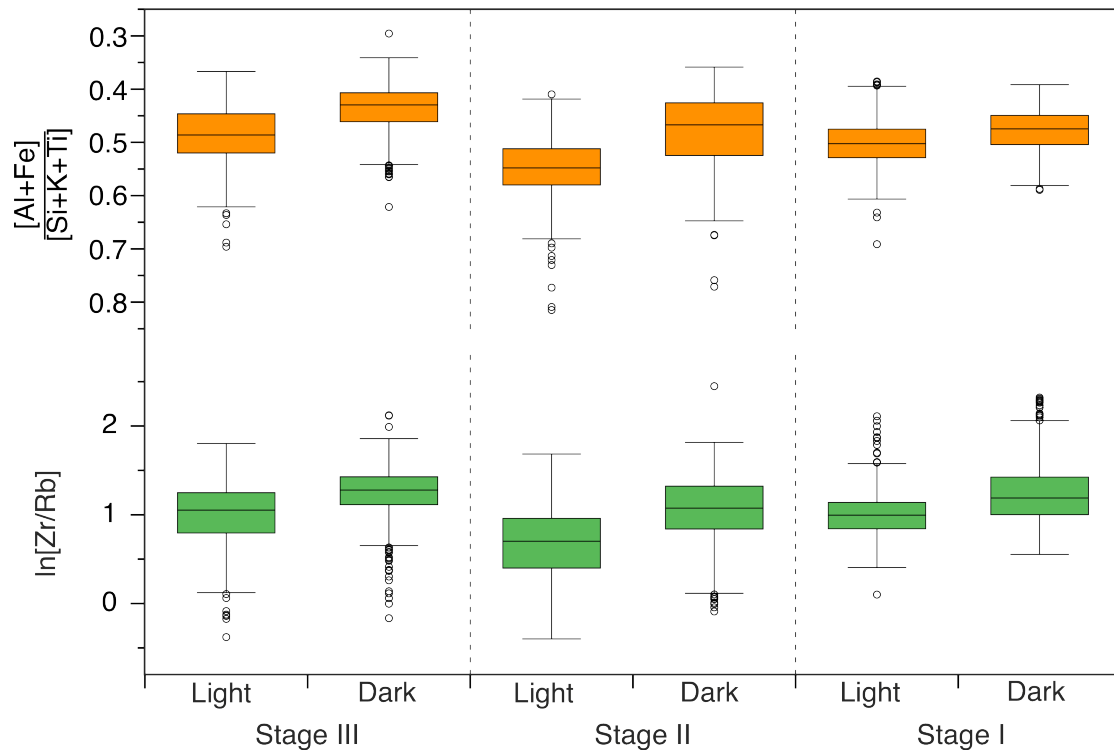
Extended Data Figure 1 | Comparison between hydroclimate proxies measured at Site 659. a, b, c Bulk sediment $[Al+Fe]/[Si+K+Ti]$ (orange), δD signatures of C_{31} n -alkanes (pale blue, 1σ error bars)^{39,40}, $\ln[Zr/Rb]$ (green, pale colours indicate low element counts). **d, e, f** Generalised additive model (GAM) fit of Site 659 $[Al+Fe]/[Si+K+Ti]$ data shown by black line with grey shaded confidence band (2 standard error). Black crosses indicate original data points with resampled data points used in Kendall's tau-b correlation tests indicated by red circles (see Supplementary Information). **a,d** late Pleistocene, **b,e** late Pliocene, **c,f** early Pliocene.



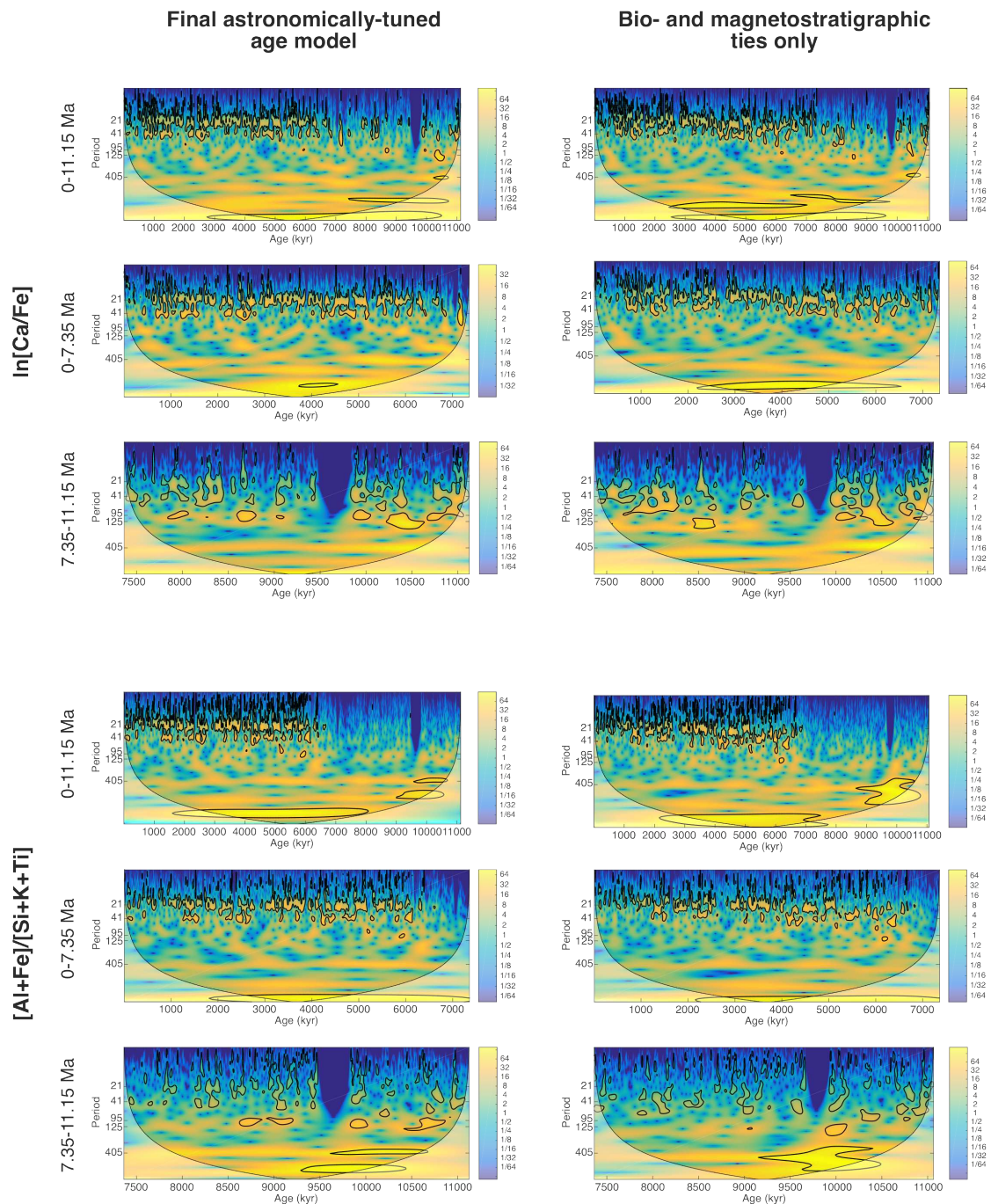
Extended Data Figure 2 | Coherency spectra comparing our data from Site 659 to published dust and hydroclimate records from the same and nearby sites. Green dashed line marks 90% Monte Carlo false-alarm level. **a & b** Coherency between the dust % estimates from Site 659 of Tiedemann et al. (1994)² and our $\ln[\text{Ca}/\text{Fe}]$ (**a**) and dust flux (**b**) estimates over the last 8 Myr. **c** Coherency between our estimated dust fluxes and those of Skonieczny et al. (2019)¹⁵ from nearby site MD03-2705 over the last 240 kyr. **d, e, f** Coherency between our $[\text{Al}+\text{Fe}]/[\text{Si}+\text{K}+\text{Ti}]$ values and C_{31} *n*-alkane δD values from Site 659 from Kuechler et al. (2013, 2018)^{39,40} for three time slices in the Quaternary (**d**) and Pliocene (**e, f**).



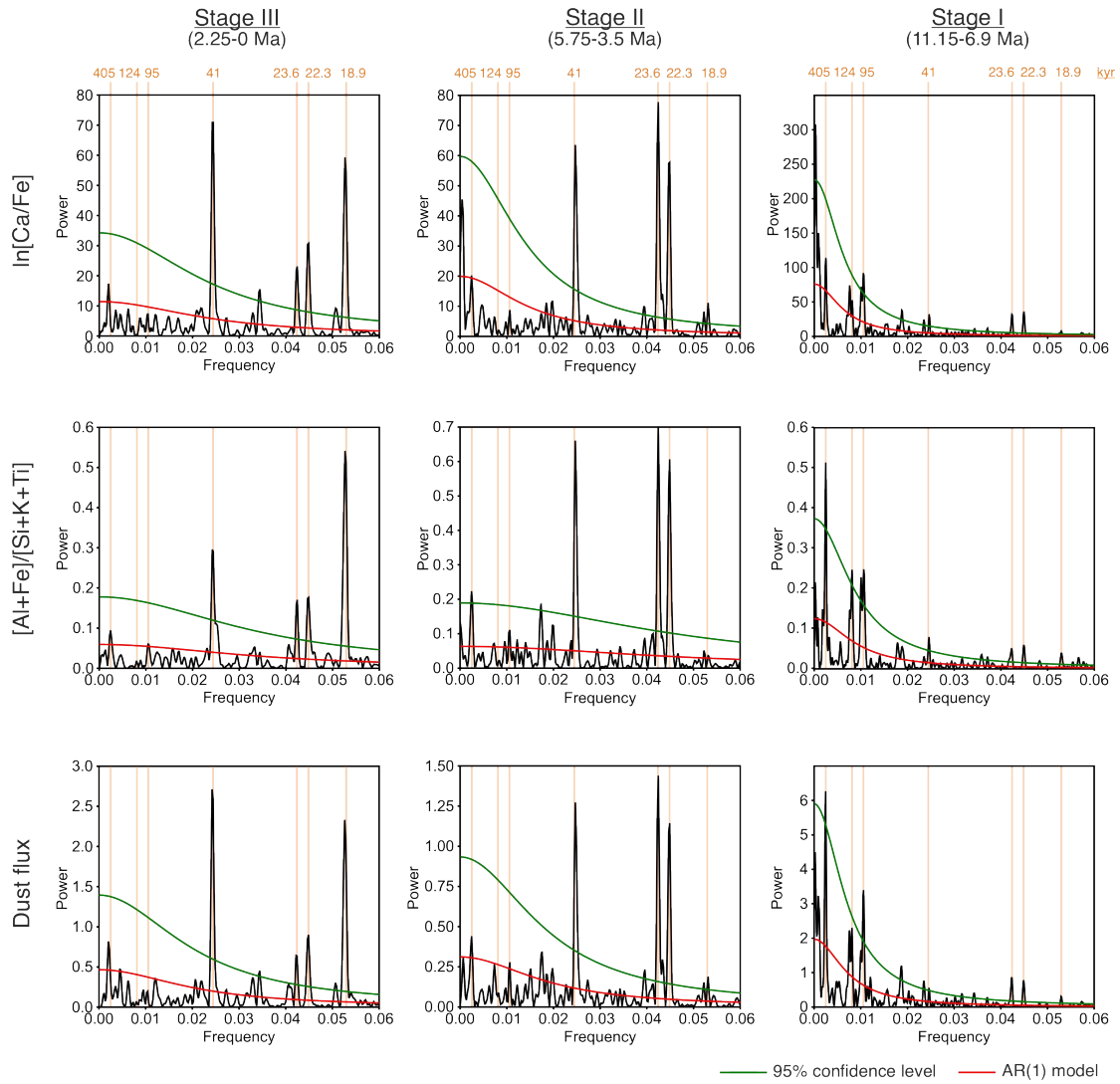
Extended Data Figure 3 | Comparison between methods for calculating dust fluxes to marine sediments over the last 250 kyr. a Red: modal dust flux estimates from Site 659 based on a geochemical end-member unmixing approach, with orange lines marking ± 1 standard deviation of 500 realizations. Blue: Dust flux estimates from site MD03-2705 (directly adjacent to Site 659) calculated by ^{230}Th normalization¹³ with error bars indicating ± 1 standard deviation. **b** Generalized Additive Model⁹⁹ fit of Site 659 median dust fluxes shown by black line with grey shaded confidence band (2 standard error). Black crosses indicate original data points with resampled data points used in Kendall's tau-b correlation tests indicated by red circles (see Supplementary Information).



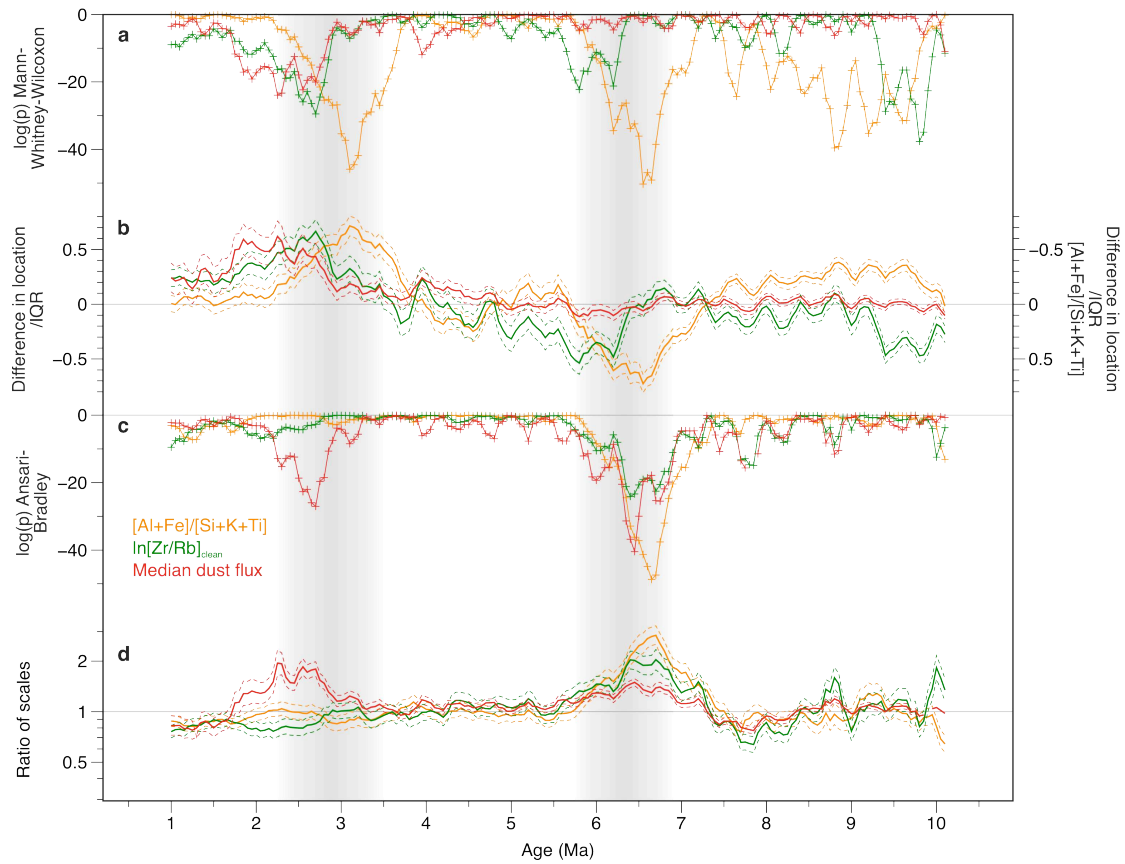
Extended Data Figure 4| Box and whisker plot illustrating co-variation in sediment colour and geochemistry at Site 659. Top: $\frac{[Al+Fe]}{[Si+K+Ti]}$, bottom: $\ln[Zr/Rb]$. Data are plotted from “light” and “dark” sediment layers (as defined by the method described in the Supplementary Information) for each of the three time stages (Stage I: 11.15 – 6.7 Ma, Stage II: 5.75 – 3.5 Ma, Stage III: 2.25 – 0 Ma). Box indicates interquartile range (IQR) with line marking median value, outliers (>1.5 IQR from median) marked with circles and whiskers drawn to the maximum/minimum values excluding outliers. Mann-Whitney-Wilcoxon tests were used to test the null hypothesis that samples from light and dark layers have identical continuous distributions with equal medians for each time interval. All resulting p -values were <0.001 , giving $>99.9\%$ confidence that the differences between light and dark layers are significant.



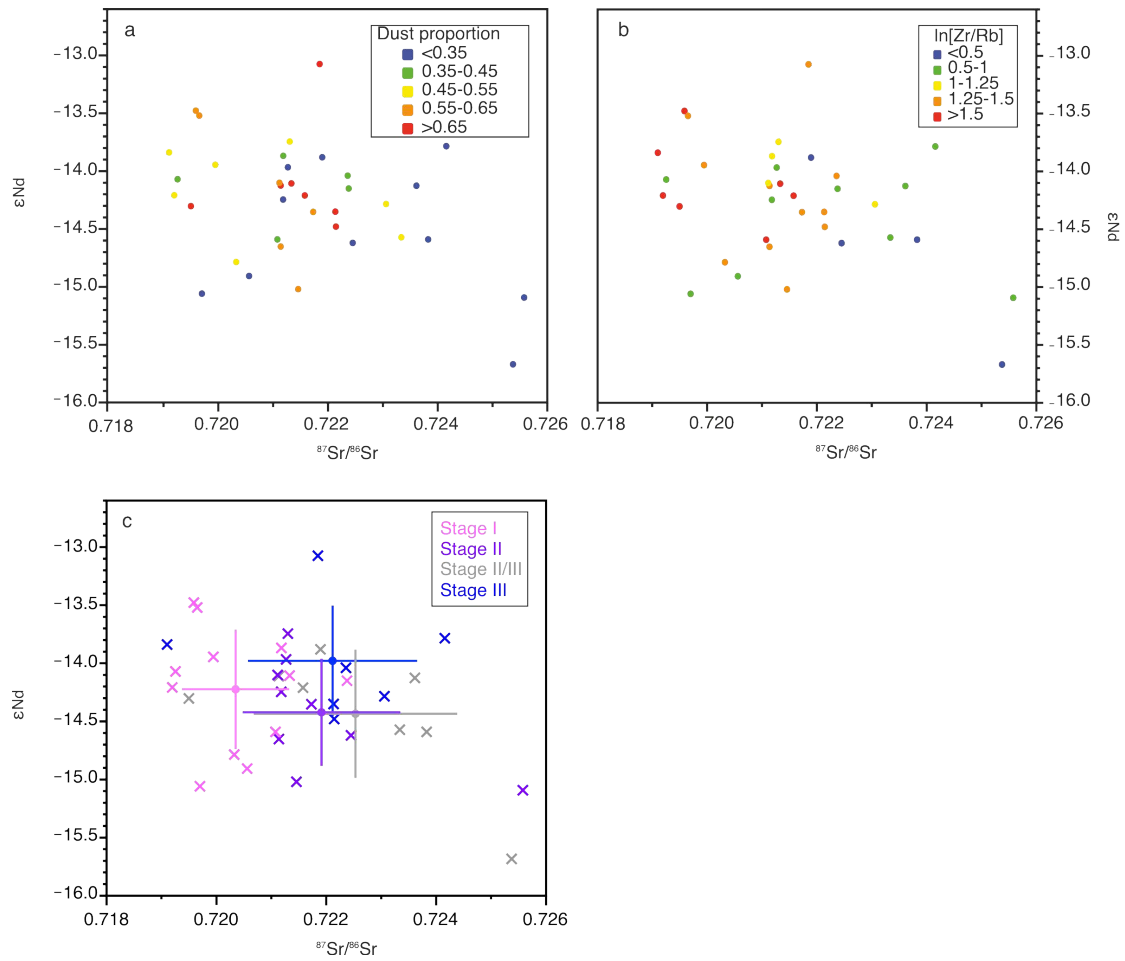
Extended Data Figure 5 | Wavelet analysis of Site 659 geochemical records. Comparison between continuous wavelet power spectra of calibrated $\ln[\text{Ca}/\text{Fe}]$ (top) and $[\text{Al}+\text{Fe}]/[\text{Si}+\text{K}+\text{Ti}]$ (bottom) data on the astronomically-tuned age model (left) and an untuned age model based solely on biostratigraphic and magnetostratigraphic datums^{14,69} (right). Thick black contours designate the 5% significance level against red noise and the cone of influence is shown as a lighter shade, where edge effects may cause distortion. Data were detrended and smoothed (5-pt moving average) prior to the wavelet analyses. Separate spectra were also generated for the older and younger sections of the full record to reduce the impact of temporal changes in cycle amplitude on the detected frequencies. Analyses were performed and figures generated using the Matlab code of Grinsted et al. (2004)¹⁰⁰. See Supplementary Information for further discussion.



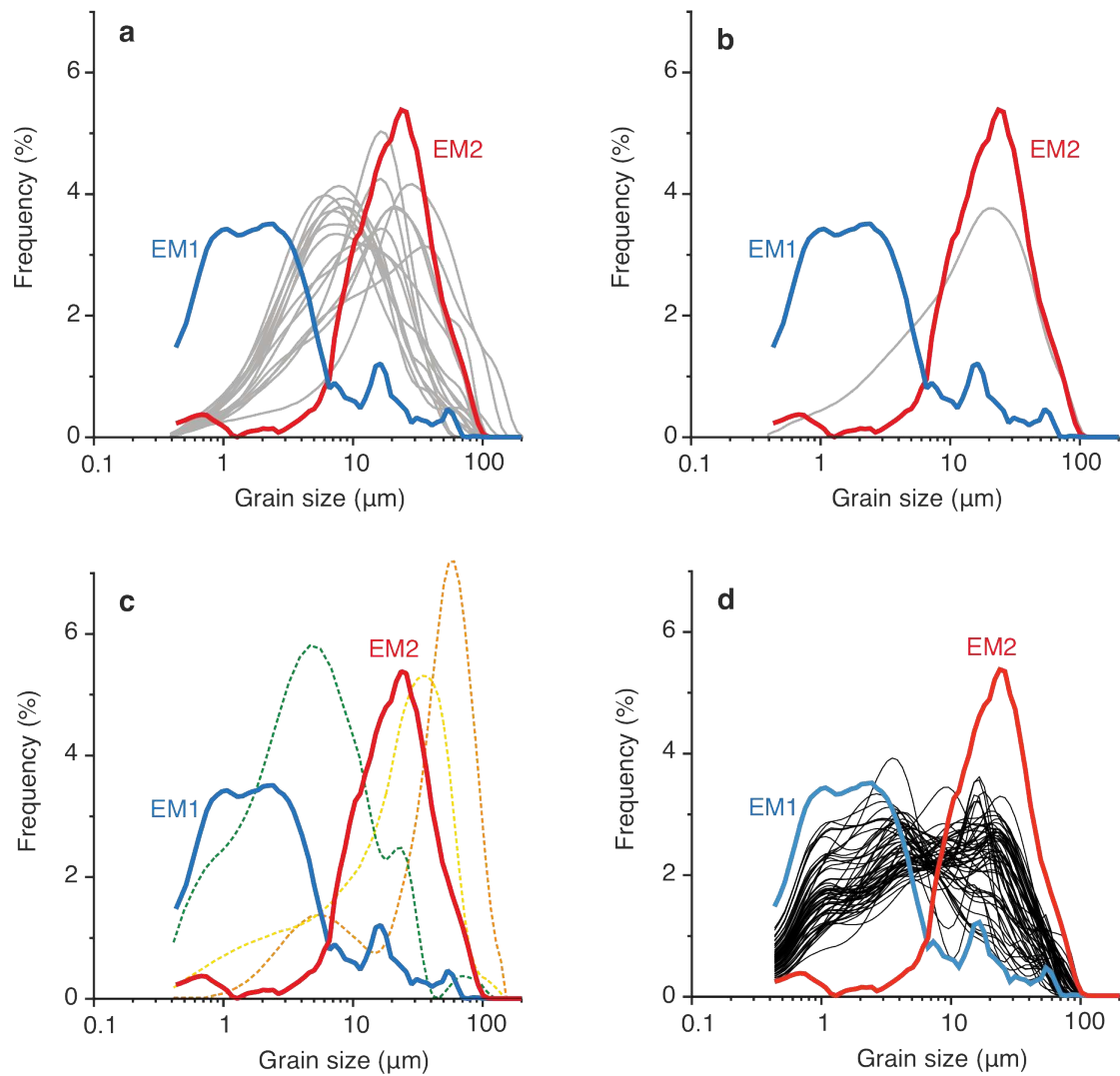
Extended Data Figure 6 | REDFIT spectral analysis⁷⁵ of Site 659 geochemical records. Top: $\ln[\text{Ca}/\text{Fe}]$ ratios, middle: calibrated $[\text{Al}+\text{Fe}]/[\text{Si}+\text{K}+\text{Ti}]$ ratios, bottom: median dust flux values. Data are divided into the three time stages discussed in the text. Left: Stage III (2.25–0 Ma), centre: Stage II (5.75–3.5 Ma), right: Stage I (11.15–6.9 Ma). Green curves mark the false-alarm level at the 95% confidence level, red curves indicate AR(1) red noise models. Orange lines and numbers indicate the frequencies equivalent to periods (in kyr) of major astronomical cycles (precession, obliquity and eccentricity). Analysis performed and figures created using PAST software¹⁰¹. See Supplementary Information for further discussion.



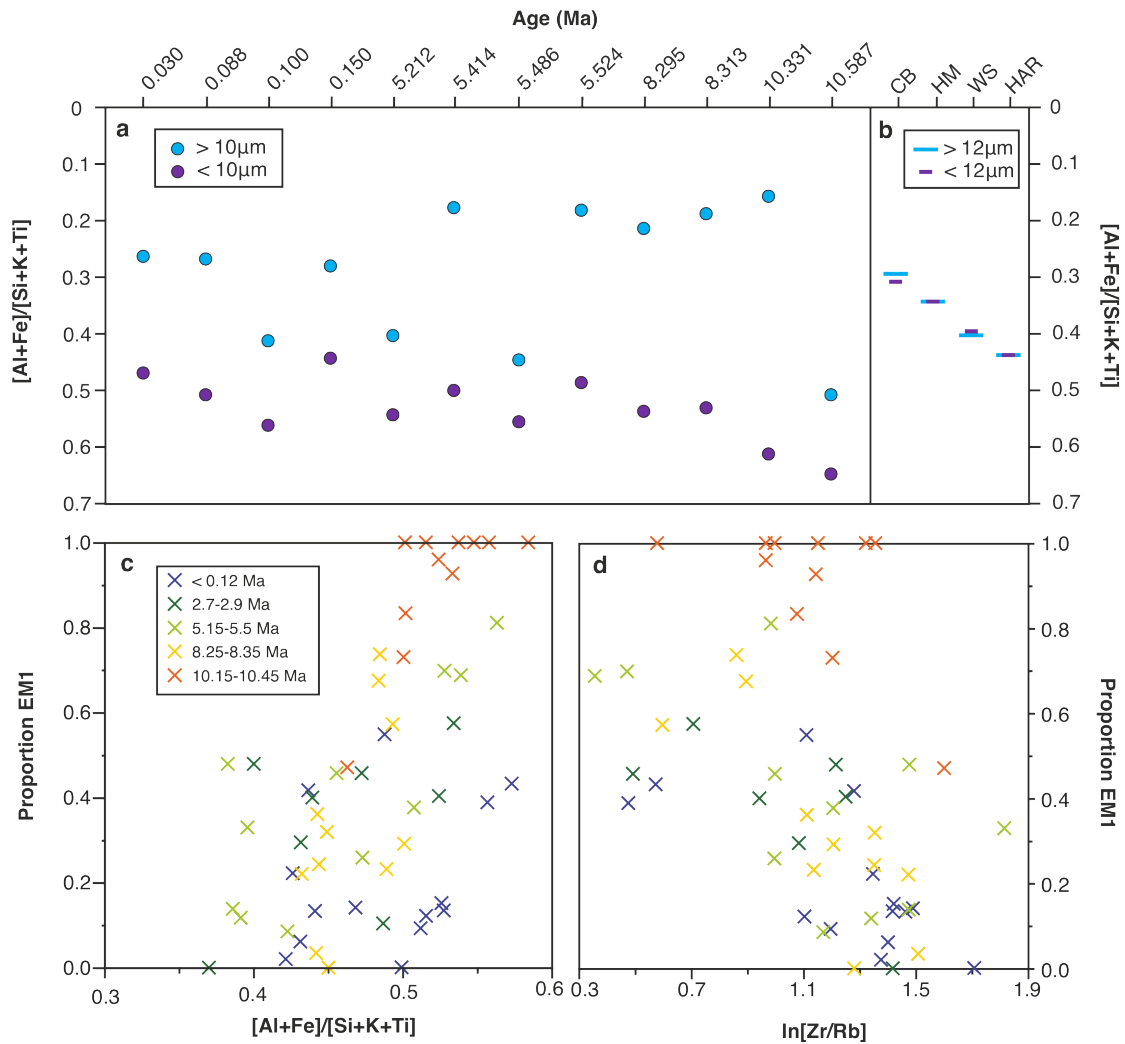
Extended Data Figure 7 | Running statistical analysis of Site 659 geochemical data, comparing 1 Myr data bins. **a** Mann-Whitney-Wilcoxon test $\log(p)$ values to detect shifts in central tendency (see Supplementary Information). Low values indicate extremely low probabilities that the two data bins have the same central tendency. **b** Estimated difference in location between the two data bins divided by the interquartile range of the complete data set, with 95% confidence interval plotted. Note that $[\text{Al}+\text{Fe}]$ is plotted on an inverted axis. **c** Ansari-Bradley test $\log(p)$ values to detect shifts in dispersion. Low values indicate extremely low probabilities that the two data bins have the same dispersion. **d** Ratio of scales between the two data bins, with 95% confidence interval plotted. Orange: calibrated $[\text{Al}+\text{Fe}]/[\text{Si}+\text{K}+\text{Ti}]$, green: $\ln[\text{Zr}/\text{Rb}]$ (with XRF counts <300 removed), red: median dust flux ($\text{g cm}^{-2} \text{ kyr}^{-1}$). Grey shading indicates intervals of greatest change in the geochemical time series revealed by statistical analyses.



Extended Data Figure 8 | Cross-plots of strontium and neodymium isotopic signature of lithic fraction of Site 659 sediments. Data coloured by: **a** the proportion of the lithic fraction attributed to dust by end-member unmixing ($[\text{dust}]/[\text{dust}+\text{riverine}]$), **b** co-registered $\ln[Zr/Rb]$ values. Red marks samples dominated by dust/coarse grains, blue marks samples dominated by riverine inputs/fine grains. **c** Data coloured by age, where stage I (pink) is the oldest (>6.9 Ma) and stage III (blue) is the youngest (<2.25 Ma) and grey indicates samples from the transition between stages II and III (3.5–2.25 Ma). Individual samples are marked by crosses and mean values for each age range shown by circles, with error bars indicating 1 standard deviation.



Extended Data Figure 9 | Grain size distributions of the end-members calculated from the lithic fraction of ODP Site 659. Grain size derived end-member 1 (EM1) in blue and grain size derived end-member 2 (EM2) in red compared to: **a** Modern dust samples recorded offshore NW Africa from Stuat et al. (2005) in grey⁶⁴. **b** As (a) but with just the most proximal measurements to Site 659 (M41/1 D4, centered at 19.73°N, 17.91°W) plotted. **c** The grain size end members of Tjallingii et al. (2008) from site GeoB7920-2 (20.75°N, 18.58°W)¹². Yellow and orange dashed lines indicate the end members attributed to fine and coarse dust respectively, with the riverine end member shown in green. **d** All Site 659 lithogenic grain size distributions (black).



Extended Data Figure 10| Comparisons between grain size and geochemical proxies at Site 659. a & b $[Al+Fe]/[Si+K+Ti]$ ratios of the coarse and fine fractions of (a) 12 sediment samples from Site 659 sieved at $10\mu m$ and analysed by discrete XRF analysis with sample ages are listed along the top and (b) desert surface soil and aeolian dusts from four locations in the Sahara-Sahel dust corridor, analysed by inductively coupled plasma mass spectrometry and grouped into $<12\mu m$ and $>12\mu m$ size fractions, from Castillo et al. (2008)¹⁰². CB: Chad Basin, HM: Hoggar Massif, WS: Western Sahara, HAR: Harmattan. c and d The proportion of lithogenic grain size derived end-member 1 (grain size EM1, attributed to fine riverine inputs) plotted against the sediment geochemical ratios c $[Al+Fe]/[Si+K+Ti]$ and d $\ln[Zr/Rb]$. Data points are coloured by sample age, where the youngest samples are in blue and the oldest in orange.

Supplementary Information

For: Astronomically controlled aridity in the Sahara since at least 11 million years ago

Anya J. Crocker, B. David A. Naafs, Thomas Westerhold, Rachael H. James, Matthew J. Cooper, Ursula Röhl, Richard D. Pancost, Chuang Xuan, Colin P. Osborne, David J. Beerling, Paul A. Wilson

Supplementary Discussion

Comparison to published dust reconstructions

Reconstructions of the flux of dust from the African continent deposited in ODP Site 659 sediments over the past 5 Myr were originally published by Tiedemann et al. (1989)¹ and Tiedemann et al. (1994)². Their records are based upon the assumption that the proportion of dust in the sediment can be approximated from the non-carbonate fraction (=100-%CaCO₃). We find an excellent correlation between the discrete measurements of these earlier studies (which include a range of analytical techniques)¹ and ln[Ca/Fe] values measured by XRF core scanning (Supplementary Figure 4). A Kendall's tau-b correlation test between the dust % estimates of Tiedemann et al. (1994)² and those presented here reveals a positive, extremely significant correlation ($\tau = 0.669$, p -value <0.001), with a comparison between published dust % to ln[Ca/Fe] revealing an even stronger (but negative) correlation ($\tau = -0.711$, p -value <0.001). These results show that our ln[Ca/Fe] data provide reliable down core records of terrigenous sediment content at ODP Site 659. We note, that these datasets, in common with many palaeoclimate records, likely show autocorrelation (where there is a degree of similarity between a time series and a lagged version of itself). This acts to elevate the calculated correlation coefficients between data series. We therefore also show coherency spectra, calculated using the REDFIT-X program of Ólafsdóttir et al. (2016)³. This approach uses a Lomb-Scargle Fourier transform to perform cross-spectral analyses between unevenly spaced data sets. Monte Carlo simulations that mimic key properties of the datasets (e.g. autocorrelation and time spacing) are used to estimate the false-alarm level for the calculated coherency. These spectra are shown in Extended Data Figure 2. Significant coherency between the dust % estimates of Tiedemann et al. (1994) and both our ln[Ca/Fe] and dust % estimates across almost all frequencies supports the strong agreement among the different techniques (Extended Data Figure 2a,b).

Recent work has shown that, in addition to dust inputs, fine-grained riverine sediment is a likely contributor to Site 659 and the nearby continental margin^{4,5}. We therefore partitioned the bulk terrigenous sediment component into two separate components (classified as riverine and aeolian) by applying an unmixing approach (Methods). Our absolute dust fluxes are therefore lower than those of Tiedemann et al. (1994)² (Supplementary Figure 4), which were calculated by assuming that all terrigenous material at Site 659 was wind-blown in origin. Nevertheless, for the last 5 Myrs, where there are detailed records from Tiedemann et al. (1994)², the down core trends in the data yielded by the two different approaches are generally very consistent over both secular and astronomical timescales.

For sediments younger than about 200 to 300 kyr, thorium-normalization of sediment accumulation rates has been used to provide age control independent of sediment focusing and dissolution along the NW African margin⁶⁻¹⁰. To assess whether these processes likely exerted a major control over our dust flux reconstructions we compared our calculated fluxes to those from site MD03-2705⁹ (18°05'N, 21°09'W). Because dust flux estimates were calculated at

different age points between the two sites, we calculated generalized additive models (GAMs)¹¹ using R¹² to create a smoothed fit to our datasets and resampled this at ages corresponding to the ²³⁰Th-normalised data points (Extended Data Figure 3). This approach provides a good representation of the original dataset, except for the most recent 20 kyr, where GAMs struggle to capture the high frequency, high magnitude variability seen at both Site 659 and MD03-2705. The degree of correlation between the two dust flux reconstructions was then assessed using a Kendall's tau-b correlation test. Despite uncertainty introduced by the GAM approximations and chronological uncertainties between the two sites, we find a positive, strongly significant correlation ($\tau = 0.298$, p -value < 0.001) between our dust fluxes at Site 659 and those calculated by ²³⁰Th-normalisation at proximal site MD03-2705⁹ (Extended Data Figure 3). We also performed cross-spectral analysis between the two datasets using REDFIT-X³ (where no resampling is required). The results of these analyses indicate that there is largely significant coherency between data sets across the frequency range 0.025–0.23 cycles/kyr (Extended Data Figure 2c), equivalent to periodicities of 40–4 kyr. These results suggest that our dust flux reconstructions are representative of aeolian transport from the continent and not major sediment redistribution in the ocean or rapid pulses of dissolution, at least over the past 240 kyr where ²³⁰Th-normalised dust flux estimates exist.

Comparison to established XRF ratios and other hydroclimate proxies

Our discussion focuses on two geochemical ratios ($[\text{Al}+\text{Fe}]/[\text{Si}+\text{K}+\text{Ti}]$ and $\ln[\text{Zr}/\text{Rb}]$) provided by our XRF work but our interpretations gain further support from three other elemental ratios that have also been shown to closely track climatic gradients along the African coastline today. Ti/Al is proposed as a proxy for aeolian versus fluvial input and Fe/K and Al/Si are suggested as tracers of terrestrial climatic zones¹³, although Al/Si can also be influenced by high siliceous microfossil concentrations at times of intense upwelling¹⁴. All three of these ratios agree very closely with one another and with $[\text{Al}+\text{Fe}]/[\text{Si}+\text{K}+\text{Ti}]$ over astronomical timescales throughout our records (Supplementary Figures 5 and 6). Dark sediment layers consistently record high $\ln[\text{Ti}/\text{Al}]$ values and low $\ln[\text{Fe}/\text{K}]$ and $\ln[\text{Al}/\text{Si}]$ values, indicating a dominance of aeolian over riverine sediment and a decrease in the intensity of chemical weathering, a trend documented with increasing aridity associated with increasing distance from the equator today¹³. These findings strongly support our interpretation that the dark sediment bands represent dust pulses associated with increased aridity throughout the last 11 Myr.

The different elemental ratios also show clear similarity over multi-million year timescales. The onset of more extreme wet events between 7 and 6 Myr can be seen in all ratios, as can a shift towards more arid conditions over the past ~3 Myr. A decrease in $\ln[\text{Al}/\text{Si}]$ through the Pliocene and Pleistocene is more pronounced than the other ratios, and, given the very low concentrations of siliceous microfossils recorded in the Site 659 sediments¹⁵, may indicate an increase in the proportion of silica-rich terrigenous material reaching the site, such as pale quartz grains from coastal sources¹⁶.

We also compare our $[\text{Al}+\text{Fe}]/[\text{Si}+\text{K}+\text{Ti}]$ and $\ln[\text{Zr}/\text{Rb}]$ data to an independent hydroclimate proxy: the hydrogen isotopic (δD) signature of *n*-alkanes (Extended Data Figure 1). These compounds are found as leaf waxes in terrestrial plants, with δD values at Site 659 suggested to largely depend upon the amount of rainfall, although differences in plant physiology (e.g. photosynthetic pathway, rooting depth and leaf anatomy) and climate (e.g. moisture source region, evaporation) can also influence plant wax δD signatures¹⁷. Extended Data Figure 1 illustrates the strong agreement between C₃₁ *n*-alkane δD values and our XRF-based hydroclimate proxies during several snapshots of the Pliocene and Pleistocene (where δD data are available)^{18,19}.

We also test the similarity between the datasets statistically. Our data and the reported δD values are from the same site but different sample sets were used so we apply GAMs to create a smoothed fit to our $[Al+Fe]/[Si+K+Ti]$ record and resample it at the matching depths to the δD data (Extended Data Figure 1d-f). Separate fits were made for 0.14–0 Ma, 3.27–3 Ma, 3.63–3.34 Ma, 4.83–4.61 Ma and 4.99–4.83 Ma to ensure that the GAMs captured astronomical-scale variability. We combined the data from all of the time windows to perform a Kendall's tau-b correlation test with the full δD dataset, which revealed a negative, strongly significant correlation with $[Al+Fe]/[Si+K+Ti]$ ($\tau = -0.218$, p -value < 0.001). Note that a negative correlation indicates agreement between the proxies, with higher $[Al+Fe]/[Si+K+Ti]$ values but more negative δD values indicating a wetter climate. The strength of the relationship between our XRF data and the δD results (Extended Data Figure 1a-c) support the use of $[Al+Fe]/[Si+K+Ti]$ to reconstruct past changes in continental hydroclimate in these sediments.

We also performed cross-spectral analysis to assess how the coherency of $[Al+Fe]/[Si+K+Ti]$ and δD varies with frequency (Extended Data Figure 2d-f). These analyses were carried out for three separate time slices due to the discontinuous nature of available high-resolution δD data. We find the strongest coherency occurs at frequencies of ~ 0.03 – 0.05 cycles/kyr, implying that these records are coherent over precessional timescales, both responding to insolation-forced variability in hydroclimate. Outside this range, the coherency is lower. This result may indicate the influence of secondary processes acting on one or both proxies over different timescales.

Geochemical differences between light and dark layers

Colour data were generated from the central portion of ODP core photograph images¹⁵ along our splice using Code for Ocean Drilling Database macros²⁰, with an average sample spacing of ~ 2 mm. Lightness values of > 80 or more than 3 standard deviations above or below a 4 cm rolling mean value were excluded to filter out artefacts such as cracks and core gaps from the dataset. Lightness data were then smoothed by calculating the mean value over a 4 cm rolling window.

To identify “light” and “dark” sediment layers, we filtered out longer-term variability in the lightness data by calculating residuals from a 5 m rolling mean. The residual dataset was then resampled to match the depths corresponding to XRF data using simple linear interpolation. “Light” layers were defined as those with residual lightness values greater than the 60% percentile of the rolling 5 m window, while dark layers were defined as those with lightness values below the 40% percentile.

Extended Data Figure 4 illustrates the geochemical differences between sedimentary layers classified as “light” and “dark” in the Site 659 XRF datasets. Mann-Whitney-Wilcoxon tests were used to identify whether there were significant geochemical differences between the light and dark layers for each of our three time intervals. Extremely low p -values (< 0.001) are documented for both $[Al+Fe]/[Si+K+Ti]$ and $\ln[Zr/Rb]$ in each of the three time windows, which shows that there are clear, highly significant geochemical differences between light and dark sediment layers at Site 659.

Identification of change points in time series

To identify the intervals of greatest change in our geochemical time series, we applied running Mann-Whitney-Wilcoxon (also known as Wilcoxon rank sum) and Ansari-Bradley statistical tests, following the approach of Trauth et al. (2009)²¹. We test whether samples taken from 1 Myr ranges either side of a selected age come from distributions with the same properties, or

whether there were significant differences between them. We used 1 Myr bins to smooth out the influence of shorter frequency astronomical variability and highlight secular changes in the datasets.

[Al+Fe]/[Si+K+Ti], $\ln[\text{Zr/Rb}]$ and median dust flux data sets were each resampled using simple linear interpolation to give an average data resolution of 2 kyr. A Mann-Whitney-Wilcoxon test was applied to test the null hypothesis that samples from the million years preceding and postdating the chosen date were selected from identical continuous distributions with equal medians.

The Ansari-Bradley test determines whether two samples come from continuous distributions with the same median and shape but different dispersions. As the results of the Mann-Whitney-Wilcoxon test indicate that there are significant shifts in the median values of all three of our proxy data sets between different time windows, we calculate the difference of each data point from the whole-core mean and then adjust these residuals by the difference in location between the two time windows (the median of the difference between a sample from each of the two distributions). Due to the size of the datasets, a normal approximation was used when calculating the p -values.

The results of the running Mann-Whitney-Wilcoxon and Ansari-Bradley tests on our three proxy datasets reveal two major intervals of change in our time series; 6.9–5.75 Ma and 3.5–2.25 Ma (Extended Data Figure 7). The first interval is marked by a major increase in the variability of all three proxy records from 6.9–6.3 Ma, accompanied by an increase in the central tendency of [Al+Fe]/[Si+K+Ti] values. This is followed by a decrease in $\ln[\text{Zr/Rb}]$ values (6.2–5.75 Ma).

During the second key interval of change, a decrease in the central tendency of [Al+Fe]/[Si+K+Ti] (centred around 3.2–3.1 Ma) again leads change in the $\ln[\text{Zr/Rb}]$ data (which shows an increase centred around 2.8–2.25 Ma), although this time there is also an increase in the mean dust flux values approximately synchronous with the change in $\ln[\text{Zr/Rb}]$. There is a shift to greater dispersion in the dust fluxes centred around 2.7 Ma, but no concurrent change in the amplitude of variability of [Al+Fe]/[Si+K+Ti] or $\ln[\text{Zr/Rb}]$.

Attribution of sedimentological end-members

Our two lithogenic grain size end-members identified at Site 659 have clearly distinct grain size distributions. End-member EM1 is by far the finer of the two, with modal grain sizes of 0.7–4 μm . End-member EM2 has a sharp, unimodal distribution dominated by grains of 10–40 μm diameter.

There is remarkable agreement between the grain size distributions of Site 659 lithogenic end-member 2 (EM2) and dust samples taken offshore NW Africa²², particularly those sampled closest to Site 659 (Extended Data Figure 9). EM2 is also similar to the fine dust end-member identified at NW African site GeoB7920-2 by Tjallingii et al. (2008)⁴ (Extended Data Figure 9). We therefore attribute EM2 to windblown dust exported from the African continent.

The origin of EM1 is less immediately obvious. Distal dusts transported long distances from their sources are suggested to have volume median grain sizes of ca. 2–7 μm ²³⁻²⁶, therefore, it is possible that EM1 at Site 659 also represents a dust component, albeit much finer than EM2. However, Site 659 end-member 1 (EM1) contains a much higher proportion of grains <2 μm than any of the atmospheric dust samples recorded offshore northwestern Africa by Stuut et al. (2005)²² (Extended Data Figure 9a), and is finer than either samples dominated by either wet or dry deposition captured by sediment traps offshore Cape Blanc²⁷. EM1 is also finer than

modern African dust captured across the Atlantic throughout the year and more distal African-sourced dust in Puerto Rico^{23,28,29}. These observations strongly suggest that EM1 is unlikely to represent a pure dust component, at least under wind conditions similar to modern.

We note that EM1 has a very strong similarity to the grain size distribution of the fine lithogenic end-members identified by both Holz et al. (2004)³⁰ and Tjallingii et al (2008)⁴, which are attributed to distal rain-out of fine particulates from riverine sources. Networks of river channels, active during past intervals of humidity have been identified across North Africa, many of which drain into the Atlantic^{5,31}, with submarine channels transporting this material into the deep ocean^{32,33}. A distal riverine interpretation for fine-grained sediments at Site 659 is supported by high proportions of the fine end-member in core top sediments offshore Morocco which receive sediment from the Souss River³⁰ and the fact that highest proportions of this fine end-member occur at times where enhanced rainfall is well evidenced in North Africa, such as African Humid Period 1^{4,34}, although increased fluxes of fine sediments are not consistently observed at all sites on the northwest African margin at this time⁸. The elevated location of Site 659 on the Cape Verde Plateau means that hypopycnal transport would likely be required for material of riverine origin to reach the site. EM1 at Site 659 is slightly finer than the riverine end-member identified at site GeoB7920-2⁴ (Extended Data Figure 9c), which is consistent with the greater distance from the continent of Site 659 compared to GeoB7920-2 and the requirement for sediment to be suspended within the water column to reach Site 659 due to its elevated position on the Cape Verde Rise (Supplementary Figure 1).

A third possible contributor to EM1 is resuspension of sediments from the continental shelf. Although shelf sediments are dominated by grains much coarser than the aeolian inputs, potentially representing relict dune fields³⁵, fine grained components are preferentially transported in nepheloid layers³⁶. Nepheloid layer activity is currently very low around Cape Verde^{37,38}, however, a contribution of these processes to Site 659 cannot be ruled out.

To further explore the origin of EM1, we test for geochemical differences between the fine and coarse components of the sediments. 12 samples with a range of ages and lithologies were wet sieved at 10 μm (close to the boundary between EM1 and EM2 dominance) to separate out the coarse and finer fractions. Samples were then oven dried and homogenized, then mixed with di-lithium tetraborate and fused to create beads. These were analysed by X-ray fluorescence using a Phillip MagiX Pro WD-XRF at the University of Southampton Waterfront Campus, NOCS, calibrated using international rock standards prepared in the same way as our samples.

All 12 of our samples show a clear offset in $[\text{Al}+\text{Fe}]/[\text{Si}+\text{K}+\text{Ti}]$ between the $>10 \mu\text{m}$ and $<10 \mu\text{m}$ size fractions (Extended Data Figure 10a). The $<10 \mu\text{m}$ $[\text{Al}+\text{Fe}]/[\text{Si}+\text{K}+\text{Ti}]$ values are 0.11–0.46 greater than the $<10 \mu\text{m}$ fraction, which means that the fine grained components plot much closer to the value of suspended sediments from the Senegal River than the coarse fractions do. The largest size fraction differences are generally recorded in the Miocene aged samples from depths with high terrigenous contents (indicated by high $\ln[\text{Fe}/\text{Ca}]$ values and a dark colour). In addition, there is a strong correlation between the relative proportions of grain-size end-members and our geochemical ratios for past dust inputs (Extended Data Figure 10c,d). High proportions of EM1 are associated with both high $[\text{Al}+\text{Fe}]/[\text{Si}+\text{K}+\text{Ti}]$ values (similar to modern riverine inputs) and low $\ln[\text{Zr}/\text{Rb}]$ values which are commonly interpreted as indicating a dominance of fine-grained clays over coarse dust^{4,39}. These results are strongly supportive of a distal riverine contribution to EM1.

We note that differences in major element compositions might also be expected between coarse and fine fractions of a purely aeolian sample due to the susceptibility of different minerals with different chemical compositions to be weathered into finer particles. However, samples of dusts and dust source sediments from across the Sahara-Sahel dust corridor show negligible offsets in $[Al+Fe]/[Si+K+Ti]$ between size fractions (Extended Data Figure 10b)⁴⁰. Therefore, we suggest that the differences we record in major element signatures between the $<10\ \mu\text{m}$ and $>10\ \mu\text{m}$ size fractions reflect inputs from multiple sources rather than size-dependent fractionation from a single source.

The higher $[Al+Fe]/[Si+K+Ti]$ values of the $<10\ \mu\text{m}$ sediment component (Extended Data Figure 10) mean that our geochemical unmixing approach acts to remove this very fine component. Therefore, even if EM1 is dominantly derived from resuspended shelf material rather than distal riverine material, the geochemical unmixing approach will still act to remove its contribution from the total lithogenic component to produce our dust flux estimates. If EM1 contains a component of fine-grained dust, then our dust flux estimates are likely to be underestimates.

In conclusion, a dominantly distal riverine origin for EM1 is indicated by: (i) grain size distribution analyses showing that EM1 is very similar to the fine end-member previously identified at higher concentrations during humid time intervals^{4,34} and at latitudes to the north of the Sahara where precipitation is higher³⁰ (ii) EM1 is much finer than either proximal or distal North African dust (including samples from as far as the Caribbean)^{22,23,29,41}, (iii) large geochemical differences between the coarse and fine fractions of Site 659 sediments are too great to be explained by size-dependent fractionation from a single source, and (iv) the current absence of major nepheloid layer activity around Cape Verde^{37,38}.

Effects of grain size on radiogenic isotope signatures

A grain size effect on Sr isotope signatures of sedimentary lithics has previously been documented including in African dust, with fine-grained samples having higher $^{87}\text{Sr}/^{86}\text{Sr}$ values, although a similar effect in Nd isotopes is not commonly observed⁴²⁻⁴⁴. We find no strong relationship between the radiogenic isotopic signature and either the proportion of dust or the grain size of the sediment as approximated by $\ln[Zr/Rb]$ (Extended Data Figure 8a,b), although we note a tendency for samples with the most radiogenic Sr and unradiogenic Nd isotope signatures to have low $\ln[Zr/Rb]$ values and be dominated by riverine inputs rather than dust (according to the results of our geochemical end-member unmixing), with the inverse also true, particularly in $\ln[Zr/Rb]$. Radiogenic Sr values may be attributed to enhanced chemical weathering under humid climates resulting in a higher proportion of fine clay minerals and micas reaching Site 659⁴². The covariation with unradiogenic ϵ_{Nd} values suggest there is also a shift in provenance, potentially attributable to transport of an increased proportion of proximal material sourced from the West African Craton transported by rivers compared to aeolian inputs, which may contain a greater contribution from the interior of the continent (or potentially Morocco, although the reported Sr isotope signatures⁴⁵ suggest this scenario is less likely).

Temporal variability in radiogenic isotope signatures

The radiogenic isotope signatures of the lithic fraction of the Site 659 sediments hint at subtle differences with sediment age, but we record no clear temporal shifts in the provenance of lithogenic material through the last 11 Myr to suggest major changes in the source regions of terrigenous sediment. The oldest samples (stage I) generally show more non-radiogenic isotope values in $^{87}\text{Sr}/^{86}\text{Sr}$ (Extended Data Figure 8c), which means that these Miocene-aged samples plot slightly closer to the Central source area than to the Western region, as defined by the currently available data⁴⁶ (Figure 4). Therefore, we infer that the strong signal of dust

inputs during stage I cannot be attributed to input from coastal sand dunes (which have previously been documented back to the Early Miocene and potentially much earlier^{47,48}) and instead indicate the presence of strong dust generating regions in the continental interior back to at least the Late Miocene.

Fidelity of an astronomically-tuned age model at Site 659

Pronounced lithological and geochemical variability is well documented at Site 659, particularly over the younger intervals, and has been linked to astronomical forcing^{2,19,49-51} (e.g. Figure 3, Supplementary Figure 6). These observations therefore provide an opportunity to capitalize on the potential to gain a high-fidelity age model for Site 659 by tuning the clear lithological cycles to an astronomical signal, as with many records of Mediterranean climate and low-latitude continental margins where a similar tuning approach has been used for chronology⁵²⁻⁵⁶. However, this approach requires care to ensure that age is assigned to our environmental records as independently as possible to guard against circularity. In our final age model, we used the core images and the ratio $\ln[\text{Ca}/\text{Fe}]$ to tune to insolation and $[\text{Al}+\text{Fe}]/[\text{Si}+\text{K}+\text{Ti}]$ and $\ln[\text{Zr}/\text{Rb}]$ as our main records of environmental change.

To assess the extent to which astronomical power is present throughout the Site 659 records, we first analysed the frequencies present in our data using wavelet analysis⁵⁷ with an age model was based solely on bio- and magnetostratigraphic datums^{15,58} and no tuning applied to the records (Extended Data Figure 5). The resulting continuous wavelet power spectrum show extremely similar patterns of variability on astronomical periodicities to our final, astronomically tuned record in both $\ln[\text{Ca}/\text{Fe}]$ and $[\text{Al}+\text{Fe}]/[\text{Si}+\text{K}+\text{Ti}]$ across the full 11 Myr datasets (Extended Data Figure 5). This result indicates that the astronomical periodicities identified in the lithology and geochemistry of Site 659 sediments are genuine and have not been artificially tuned into the data. We also note that significant power is often detected concurrently at two or more frequencies, with the ratios between these frequencies matching those of major astronomical cycles (Extended Data Figures 5 and 6). This result would be very difficult to tune into our records artificially, providing further evidence for the lithological and geochemical variability at Site 659 being astronomically-paced.

Changing astronomical pacing of hydroclimate variability in North African over the past 11 Myr

To assess how the dominant frequencies of variability change throughout our >11 Myr records, we performed spectral analysis on our $\ln[\text{Ca}/\text{Fe}]$, $[\text{Al}+\text{Fe}]/[\text{Si}+\text{K}+\text{Ti}]$ and dust flux data using REDFIT⁵⁹ to identify significant periodicities in our unevenly spaced data series (Extended Data Figure 6). Analyses were carried out using the PAST software⁶⁰

REDFIT analysis reveals a strong signature of precession throughout the last 11 Myr in $\ln[\text{Ca}/\text{Fe}]$, $[\text{Al}+\text{Fe}]/[\text{Si}+\text{K}+\text{Ti}]$ and dust flux data from Site 659 (Extended Data Figure 6), with obliquity also present in all three time intervals examined (stages I to III). Significant eccentricity is only recorded during stage I (>6.9 Ma), rather than the youngest 800 kyr when strong 100 kyr glacial cycles are recorded in benthic oxygen isotope records⁶¹. The signatures of obliquity and precession are seen in all three stages of our record, but are generally weakest in the oldest part of the record (stage I), likely, at least in part, because of the stronger smoothing effects of bioturbation where sedimentation rates are lower (Supplementary Figure 2).

The relative importance of high and low latitude forcing in driving African hydroclimate, particularly during the Quaternary Period, is debated^{2,9,62-67}. The strong presence of precessional frequencies (23 and 19 kyr) in our data (Extended Data Figure 6) supports a major role for insolation forcing of the West African monsoon. Obliquity (41 kyr) is also

strongly present, which may indicate that the ice volume at high latitudes also exerts a major control on North African hydroclimate, perhaps by influencing wind strength. However, obliquity can also influence low latitude hydroclimate directly through modulation of the cross-equatorial insolation gradient⁶⁸. The absence of an obvious strengthening of the obliquity signature associated with increasing amplitude of glacial-interglacial cycles in the Late Pliocene/early Pleistocene⁶¹ in our hydroclimate proxy $[Al+Fe]/[Si+K+Ti]$ (e.g. Extended Data Figure 5) supports this interpretation. The signal of obliquity in the latest Pliocene/Pleistocene appears slightly stronger in the $\ln[Ca/Fe]$ and dust flux records than $[Al+Fe]/[Si+K+Ti]$ which may indicate the influence of glacial-interglacial shifts in overturning circulation bringing more corrosive bottom waters to the site driving carbonate dissolution⁹ and/or higher latitude forcing exerting a stronger control over wind strength (and hence dust transport) than continental hydroclimate.

Interpreting plant wax history at Site 659

Long-chain *n*-alkanes originating from the epicuticular leaf waxes of terrestrial plants can be removed from the leaf surface by the action of wind or rain and transported to the ocean via both dust and rivers⁶⁹⁻⁷¹. A strong correlation between concentrations of *n*-alkanes and dust percentages at Site 659 suggests that transport by wind is the dominant process at this location^{2,19}. The source regions of plant waxes are likely very similar to those of the terrigenous material reaching Site 659, however, given the very low net primary production across much of North Africa, the plant wax signature may be biased to areas with higher biomass densities, particularly during arid time intervals.

Previous studies suggest that Site 659 records plant waxes dominantly sourced from the northern Sahel, with biomarker and pollen records suggesting a minor additional input of terrestrial material transported by the northeast trade winds from more northerly latitudes, evidenced during times of aridity and increased trade wind strength such as the Last Glacial Period, but not during the warmer and wetter Pliocene^{18,19,72,73}. The Sahel is currently dominated by C₄ grasslands, while the vegetation in northernmost Africa is instead dominated by C₃ plants⁷⁴. Therefore, the northwest African margin currently receives a mixture of plant waxes from these two sources. Several studies^{72,75} estimate approximately equal proportions of inputs from C₄ and C₃ plants to recent and Late Quaternary aged marine sediments around the latitude of Site 659, however other, more recent studies point to a much higher contribution from C₄ plants^{18,76}.

Combined evidence from plant wax carbon isotopes and pollen indicates C₄ savanna grasslands directly replaced savannas dominated by C₃ grasses in both eastern and southern Africa as C₄ vegetation expanded through the Neogene^{77,78}. Evidence of Poaceae (grasses) in the Niger delta as far back as the early Miocene⁷⁹ suggests a similar sequence of events unfolded in the Sahel, with a gradational increase in plant wax $\delta^{13}C$ of ca. 10 ‰ at Site 659 indicating an expansion of C₄ vegetation starting approximately 10 Myr ago⁸⁰. Superimposed on this shift (at least during the Pliocene and Late Quaternary where high-resolution data exist) is variability in $\delta^{13}C$ driven by precession, obliquity and eccentricity¹⁹. These cycles have a typical magnitude of 0.5–2.5 ‰, much smaller than the multi-million year trend in plant wax $\delta^{13}C$ (Figure 2, Supplementary Figure 3).

We note that the relatively muted signature of astronomically-forced variability recorded at Site 659 is not observed at all locations across North Africa. Some localities record variability in plant wax $\delta^{13}C$ of >8 ‰ over astronomical timescales⁸¹⁻⁸⁶, most commonly records from lakes in East Africa where the topography can lead to diverse ecosystems in closer proximity to one another than further west. Lacustrine sediments also typically record larger variability in plant wax $\delta^{13}C$ than distal marine sediment cores⁸⁷ because lake archives document more

proximal vegetation sources, can be influenced by local tectonics and hydrography particularly in tectonically active regions such as East Africa, and may also be biased by microbially-derived *n*-alkanes⁸⁷. Marine records integrate source material from across a large region and are less sensitive to subtle vegetation shifts than lake records although they can be influenced by transport processes^{19,87}.

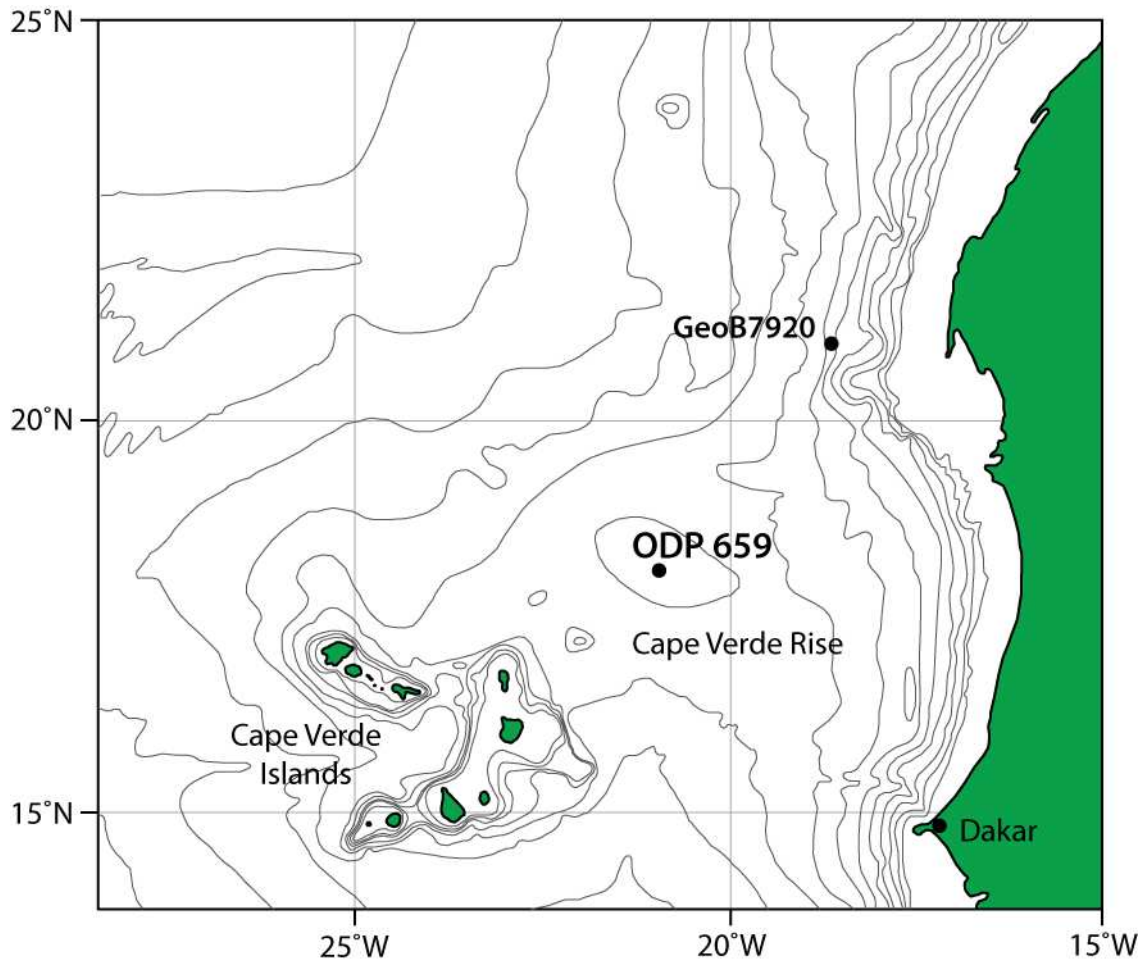
A larger range of variability in *n*-alkane $\delta^{13}\text{C}$ in the Late Quaternary than Site 659 is also recorded at northwest African margin sites GeoB9508-5 (15.5°N, -21.2 to -26.5 ‰, ~65–100 % C₄)⁷⁶ and GeoB9528-3 (9.2°N, -21.8 to -28 ‰, ~55–100 % C₄)⁸⁸ (21.0°N, -23 to -25.7 ‰, ~70–90% C₄). Both GeoB9508-5 and GeoB9528-3 lie further south and closer to the continent than Site 659. Therefore, a scarcity of sources of waxes carrying very low carbon isotopic signatures in the Sahara due to a regional dominance of C₄ vegetation could be responsible for low amplitude variability in $\delta^{13}\text{C}$ at Site 659. That said, we note that the amplitude of astronomically-forced variability in *n*-alkane $\delta^{13}\text{C}$ at both GeoB9508-5 and GeoB9528-3 is only around half the magnitude of the multi-million year shift associated with C₄ grassland expansion. We also observe that the magnitude of astronomically-forced variability in $\delta^{13}\text{C}$ at Site 659 appears slightly smaller in the Pliocene than in the Last Glacial Cycle, despite lower $\delta^{13}\text{C}$ values indicating a greater proportion of C₃ plants in the older time period (Figure 2, Supplementary Figure 3). The *n*-alkane $\delta^{13}\text{C}$ data from the Late Miocene are not of sufficient resolution to assess the magnitude of astronomically-forced variability, however we do not observe an obvious relationship between $\delta^{13}\text{C}$ and our geochemical ratios to suggest that there was strong aridity-driven cyclicality at a time when isotopic signatures indicate significant inputs from both C₃ and C₄ plants.

In summary, we conclude that it is unlikely that the muted astronomically-forced variability in $\delta^{13}\text{C}$ recorded in both the Pliocene and Quaternary at Site 659 (compared to the high amplitude astronomically-forced changes in hydroclimate) can simply be explained by the absence of a C₃ plants in the regions of Northern Africa sampled by our records.

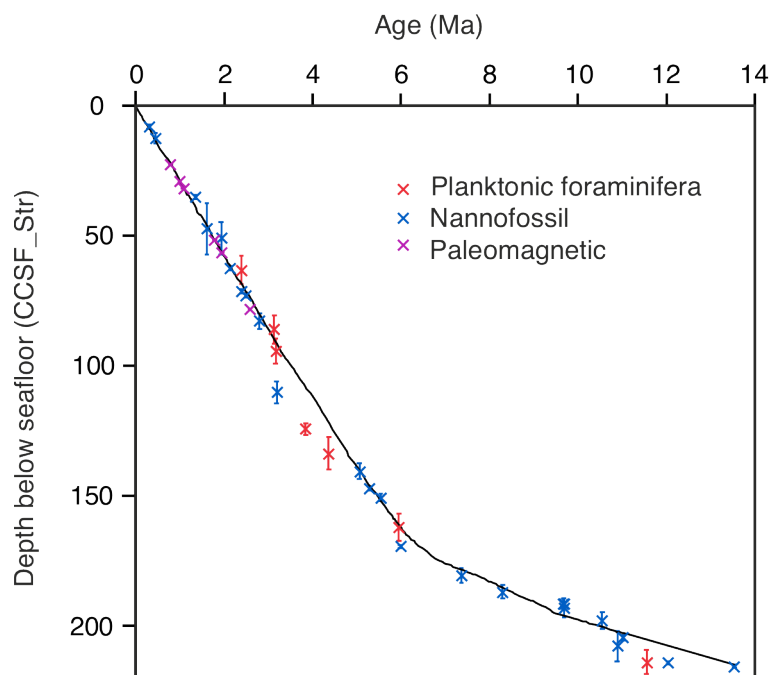
References for $p\text{CO}_2$ reconstructions

- Badger et al. (2013)⁸⁹
- Badger et al. (2019)⁹⁰
- Bartoli et al. (2011)⁹¹
- Bolton et al. (2016)⁹²
- Chalk et al. (2017)⁹³
- de la Vega et al. (2020)⁹⁴
- Dyez et al. (2018)⁹⁵
- Hönisch et al. (2009)⁹⁶
- Martinez-Boti et al. (2015)⁹⁷
- Pagani et al. (2005)⁹⁸
- Pagani et al. (2010)⁹⁹
- Seki et al. (2010)¹⁰⁰
- Sosdian et al. (2018)¹⁰¹
- Stap et al. (2016)¹⁰²
- Super et al. (2018)¹⁰³
- Tanner et al. (2020)¹⁰⁴
- Zhang et al. (2013)¹⁰⁵
- Zhang et al. (2017)¹⁰⁶
- Zhang et al. (2019)¹⁰⁷

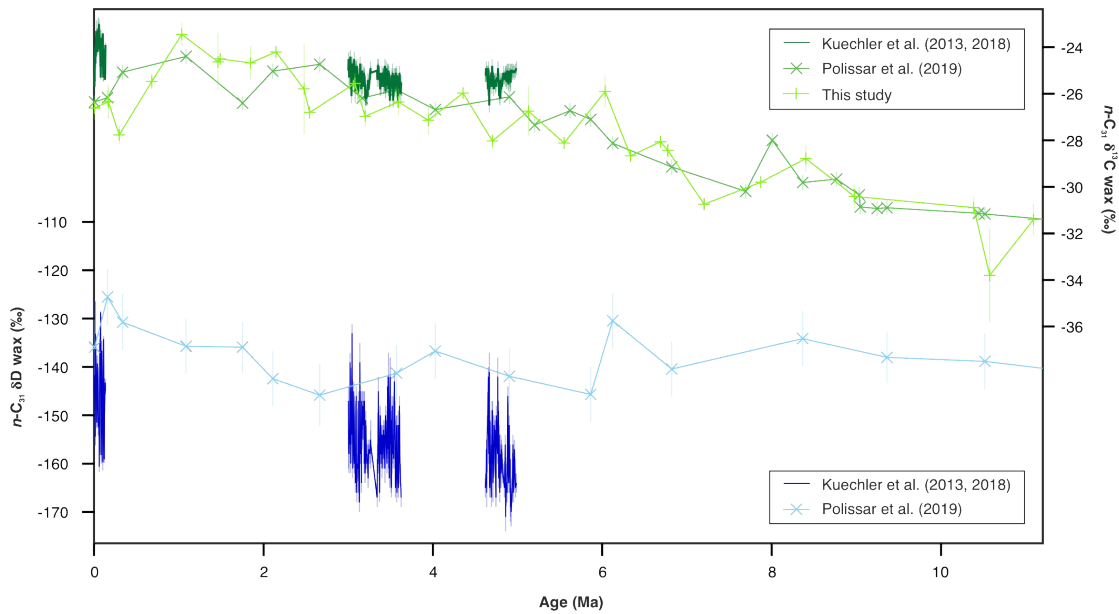
Supplementary Figures



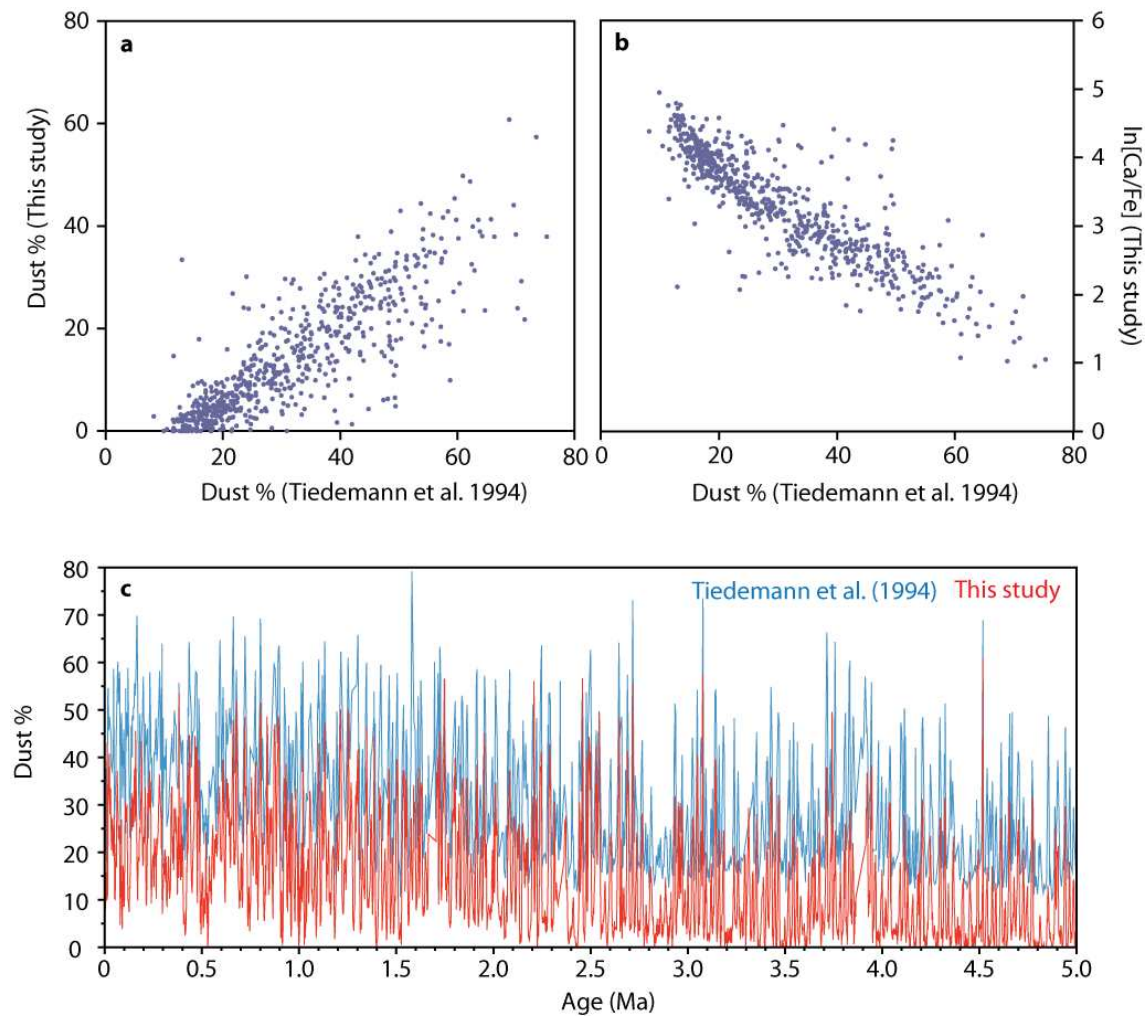
Supplementary Figure 1 | Map indicating the location of ODP Site 659 and nearby site GeoB7920, offshore NW Africa. Site locations marked by black circles, adapted from Ruddiman et al. (1989)¹⁵.



Supplementary Figure 2| Age depth plot for ODP Site 659. Age model created by benthic oxygen isotope correlation and orbital tuning used in this study (black line) compared to the original datums^{58,108} (J. Backman pers. comm.), with depths converted onto the new splice and out-of-splice sections stretched to correlate to the splice where necessary using XRF data, bulk properties and core images. Biostratigraphic and magnetostratigraphic ages updated following Raffi et al. (2006)¹⁰⁹, Wade et al. (2011)¹¹⁰ & Ogg (2012)¹¹¹. Red crosses: planktonic foraminiferal datums, blue: nannofossil datums, purple: paleomagnetic reversals.

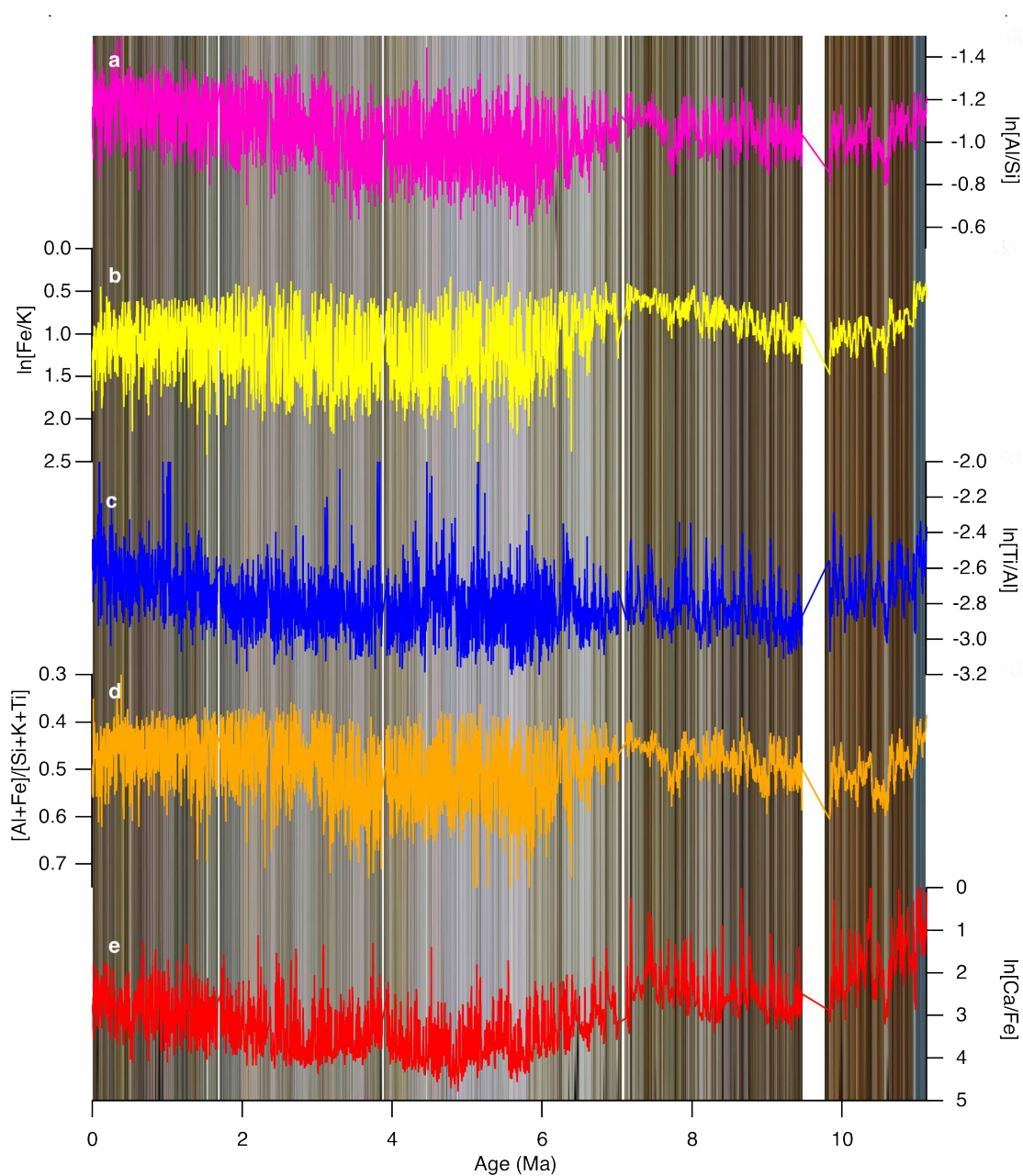


Supplementary Figure 3| Comparison of astronomically-forced variability and multi-million year trends in plant wax isotopes at Site 659. Top: $\delta^{13}\text{C}$ of C_{31} n -alkanes, data from Kuechler et al. (2013, 2018, line only)^{18,19}, Polissar et al (2019, crosses)⁸⁰ and this study (plusses). Bottom: δD of C_{31} n -alkanes, data from Kuechler et al. (2013, 2018, line only)^{18,19} and Polissar et al (2019, crosses)⁸⁰. Error bars indicate 1 s.e.m in the data of Polissar et al. (2019) and 1 sd in the data from both Kuechler et al. (2013, 2018) and this study.

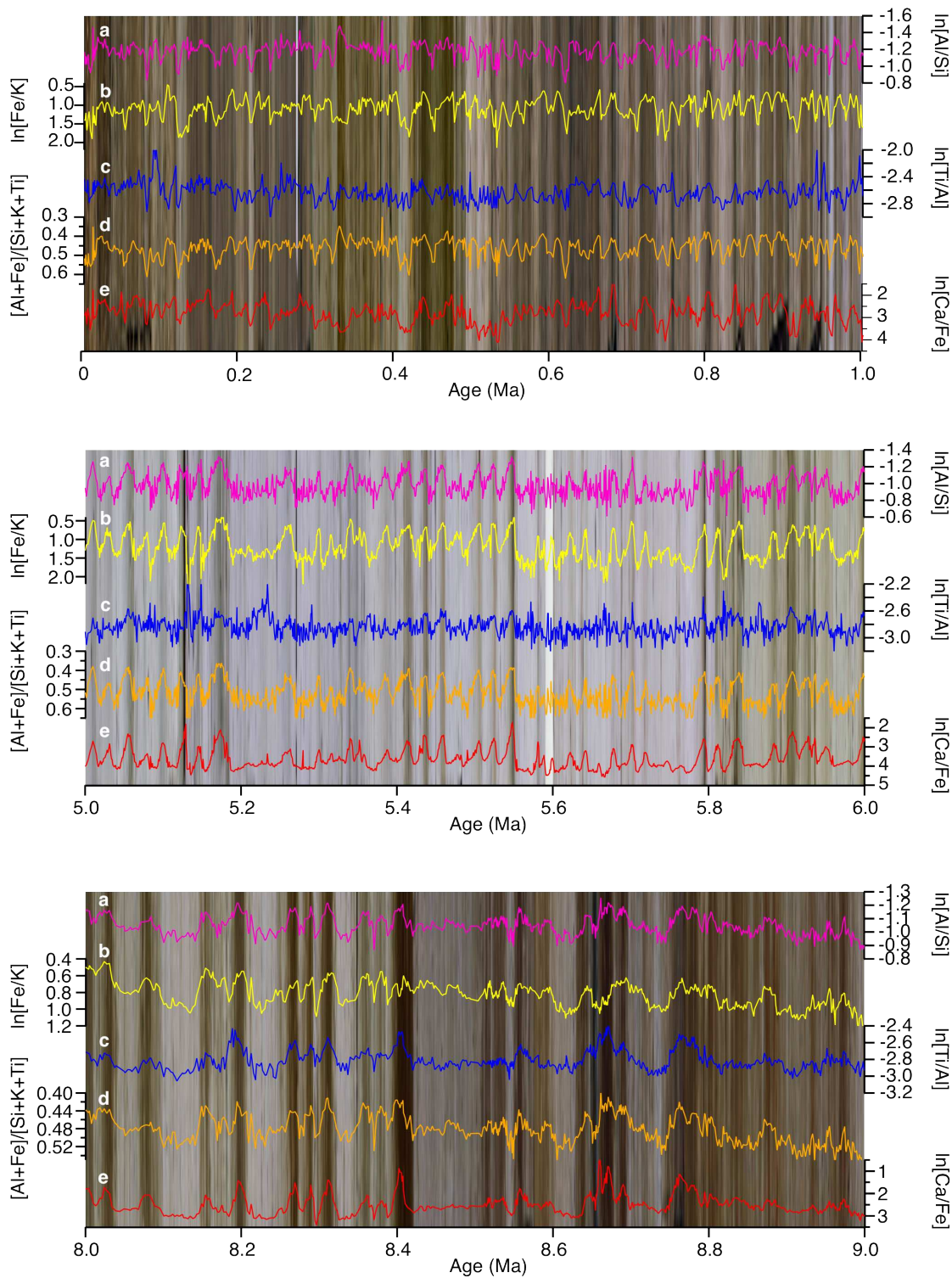


Supplementary Figure 4| Comparison of techniques for dust estimation at Site 659.

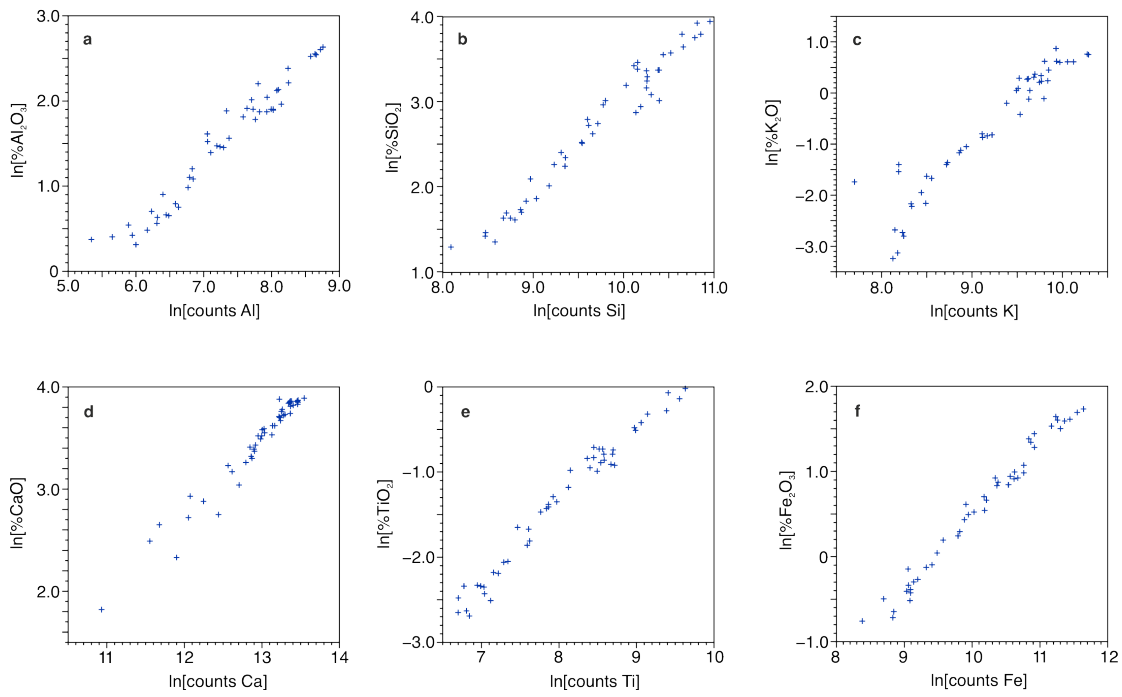
Cross-plots of dust content as a percentage of the total sediment from Tiedemann et al. (1994)² plotted against: **a** % dust estimated by end-member unmixing (this study) and **b** $\ln[Ca/Fe]$ measured by XRF core scanning (this study). Measurements included in these plots were taken within 1 cm of each other. **c** Down core records of dust as a % of the total sediment by Tiedemann et al. 1994² (blue) and this study (red), from 0–5 Ma. All data have been converted onto the splice and age model developed in this study.



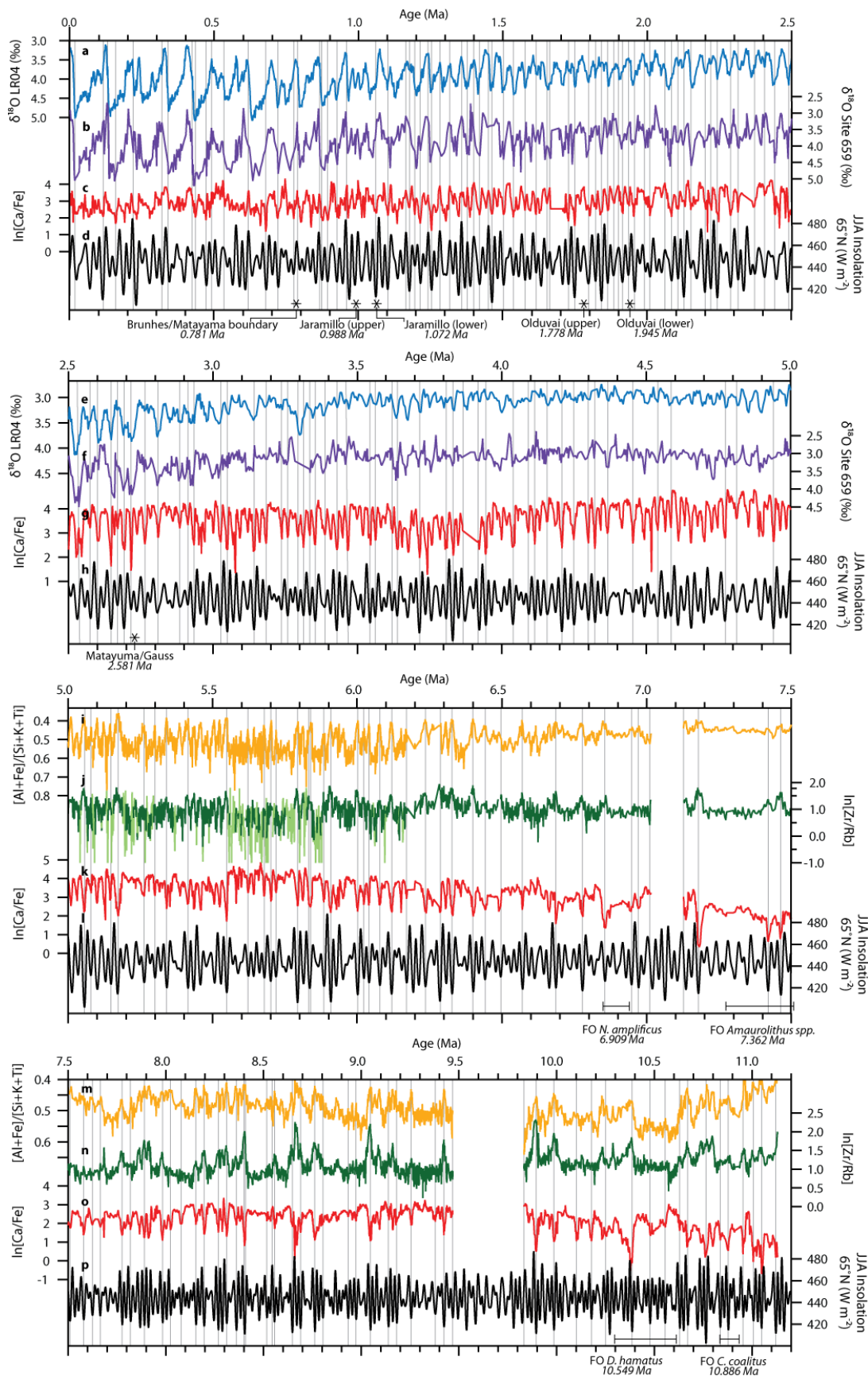
Supplementary Figure 5 Comparison of calibrated XRF ratios of Site 659 sediments spanning 0–11.2 Ma. **a** $\ln[\text{Al}/\text{Si}]$, **b** $\ln[\text{Fe}/\text{K}]$, **c** $\ln[\text{Ti}/\text{Al}]$, **d** $[\text{Al}+\text{Fe}]/[\text{Si}+\text{K}+\text{Ti}]$, **e** $\ln[\text{Ca}/\text{Fe}]$. Background image is a composited core photograph.



Supplementary Figure 6 | Comparison of snapshots of calibrated XRF ratios of Site 659 sediment, with an example from each of zone I–III. Top: 0–1 Ma, middle 5–6 Ma, bottom 8–9 Ma. **a** $\ln[\text{Al}/\text{Si}]$, **b** $\ln[\text{Fe}/\text{K}]$, **c** $\ln[\text{Ti}/\text{Al}]$, **d** $[\text{Al}+\text{Fe}]/[\text{Si}+\text{K}+\text{Ti}]$, **e** $\ln[\text{Ca}/\text{Fe}]$. Background images are composited core photographs.



Supplementary Figure 7 | Comparison of measurements of major element abundances in the calibration sample set between Avaatech XRF core scanner counts and oxide concentrations measured by discrete sample XRF analysis. **a** Al, **b** Si, **c** K, **d** Ca, **e** Ti and **f** Fe.



Supplementary Figure 8 | Stratigraphic tie-points used in the construction of the Site 659 age model. **a,e** LR04 benthic foraminiferal oxygen isotope stack⁶¹. **b,f** Site 659 *C. wullerstorfi* oxygen isotope values² converted onto our new composite depth scale and age model. **c,g,k,o** Calibrated ln[Ca/Fe] values of Site 659 sediments. **d,h,l,p** Mean boreal summer insolation (June-August) at 65°N given by the La2004 orbital solution¹¹². **i,m** Calibrated

[Al+Fe]/[Si+K+Ti] ratios of Site 659 bulk sediment. **j,n** $\ln[Zr/Rb]$ values of Site 659 sediments (pale colour indicates low counts). Grey vertical lines mark the position of tie points used to generate the age model. The position of magnetostratigraphic boundaries as identified in the Leg 108 Scientific Results¹⁰⁸ are marked by stars, with listed ages from the Geologic Time Scale 2012 (GTS2012)¹¹¹, and biostratigraphic events (as identified in the Leg 108 Scientific Results⁵⁸ and J. Backman pers. comm.) are marked by bars, with ages updated following Raffi et al. (2006)¹⁰⁹. Magnetostratigraphic and biostratigraphic dates were used to guide tuning.

References for Supplementary Information

- 1 Tiedemann, R., Sarnthein, M. & Stein, R. in *Proceedings of the Ocean Drilling Program, Scientific Results*. Vol. 108, 241-277 (ODP, 1989).
- 2 Tiedemann, R., Sarnthein, M. & Shackleton, N. J. Astronomic timescale for the Pliocene Atlantic $\delta^{18}\text{O}$ and dust flux records of Ocean Drilling Program Site 659. *Paleoceanography* **9**, 619-638 (1994).
- 3 Ólafsdóttir, K. B., Schulz, M. & Mudelsee, M. REDFIT-X: Cross-spectral analysis of unevenly spaced paleoclimate time series. *Computers & Geosciences* **91**, 11-18 (2016).
- 4 Tjallingii, R. *et al.* Coherent high- and low-latitude control of the northwest African hydrological balance. *Nature Geosci* **1**, 670-675 (2008).
- 5 Skonieczny, C. *et al.* African humid periods triggered the reactivation of a large river system in Western Sahara. *Nat Commun* **6**, 8751 (2015).
- 6 Francois, R., Frank, M., Rutgers van der Loeff, M. M. & Bacon, M. P. 230Th normalization: An essential tool for interpreting sedimentary fluxes during the late Quaternary. *Paleoceanography* **19** (2004).
- 7 Adkins, J., deMenocal, P. & Eshel, G. The “African humid period” and the record of marine upwelling from excess 230Th in Ocean Drilling Program Hole 658C. *Paleoceanography* **21**, PA4203 (2006).
- 8 McGee, D., deMenocal, P. B., Winckler, G., Stuut, J. B. W. & Bradtmiller, L. I. The magnitude, timing and abruptness of changes in North African dust deposition over the last 20,000 yr. *Earth and Planetary Science Letters* **371-372**, 163-176 (2013).
- 9 Skonieczny, C. *et al.* Monsoon-driven Saharan dust variability over the past 240,000 years. *Science Advances* **5**, eaav1887 (2019).
- 10 Kinsley, C. W. *et al.* Orbital- and Millennial-Scale Variability in Northwest African Dust Emissions Over the Past 67,000 years. *Paleoceanography and Paleoclimatology* **36**, e2020PA004137 (2022).
- 11 Wood, S. N. *Generalized additive models: an introduction with R*. (CRC press, 2017).
- 12 R: A language and environment for statistical computing. <https://www.R-project.org/> (Vienna, Austria, 2020).
- 13 Govin, A. *et al.* Distribution of major elements in Atlantic surface sediments (36°N–49°S): Imprint of terrigenous input and continental weathering. *Geochemistry, Geophysics, Geosystems* **13**, Q01013 (2012).
- 14 Meckler, A. N. *et al.* Deglacial pulses of deep-ocean silicate into the subtropical North Atlantic Ocean. *Nature* **495**, 495-498 (2013).
- 15 Ruddiman, W. F., Sarnthein, M., Baldauf, J. G. & *et al.* *Proc. ODP, Init. Repts., 108*. (ODP, 1989).
- 16 Tjallingii, R. *Application and quality of X-ray fluorescence core scanning in reconstructing late Pleistocene NW African continental margin sedimentation patterns and paleoclimate variations* PhD thesis, University of Bremen, (2006).
- 17 Sachse, D. *et al.* Molecular Paleohydrology: Interpreting the Hydrogen-Isotopic Composition of Lipid Biomarkers from Photosynthesizing Organisms. *Annual Review of Earth and Planetary Sciences* **40**, 221-249 (2012).
- 18 Kuechler, R. R., Schefuß, E., Beckmann, B., Dupont, L. & Wefer, G. NW African hydrology and vegetation during the Last Glacial cycle reflected in plant-wax-specific hydrogen and carbon isotopes. *Quaternary Science Reviews* **82**, 56-67 (2013).
- 19 Kuechler, R. R., Dupont, L. M. & Schefuß, E. Hybrid insolation forcing of Pliocene monsoon dynamics in West Africa. *Climate of the Past* **14**, 73-84 (2018).
- 20 Wilkens, R. H. *et al.* Revisiting the Ceara Rise, equatorial Atlantic Ocean: isotope stratigraphy of ODP Leg 154 from 0 to 5 Ma. *Clim. Past* **13**, 779-793 (2017).
- 21 Trauth, M. H., Larrasoána, J. C. & Mudelsee, M. Trends, rhythms and events in Plio-Pleistocene African climate. *Quaternary Science Reviews* **28**, 399-411 (2009).
- 22 Stuut, J.-B. *et al.* Provenance of present-day eolian dust collected off NW Africa. *Journal of Geophysical Research: Atmospheres* **110**, D04202 (2005).
- 23 Reid, J. S. *et al.* Comparison of size and morphological measurements of coarse mode dust particles from Africa. *Journal of Geophysical Research: Atmospheres* **108(D19)**, 8593 (2003).
- 24 Arimoto, R., Ray, B. J., Lewis, N. F., Tomza, U. & Duce, R. A. Mass-particle size distributions of atmospheric dust and the dry deposition of dust to the remote ocean. *Journal of Geophysical Research: Atmospheres* **102**, 15867-15874 (1997).
- 25 Maher, B. A. *et al.* Global connections between aeolian dust, climate and ocean biogeochemistry at the present day and at the last glacial maximum. *Earth-Science Reviews* **99**, 61-97 (2010).
- 26 Rea, D. K. The paleoclimatic record provided by eolian deposition in the deep sea: The geologic history of wind. *Reviews of Geophysics* **32**, 159-195 (1994).
- 27 Friese, C. A. *et al.* Environmental factors controlling the seasonal variability in particle size distribution of modern Saharan dust deposited off Cape Blanc. *Aeolian Research* **22**, 165-179 (2016).

- 28 van der Does, M., Pourmand, A., Sharifi, A. & Stuut, J.-B. W. North African mineral dust across the
tropical Atlantic Ocean: Insights from dust particle size, radiogenic Sr-Nd-Hf isotopes and rare earth
29 elements (REE). *Aeolian Research* **33**, 106-116 (2018).
- van der Does, M., Korte, L. F., Munday, C. I., Brummer, G.-J. A. & Stuut, J.-B. W. Particle size traces
modern Saharan dust transport and deposition across the equatorial North Atlantic. *Atmospheric
30 Chemistry and Physics* **16**, 13697 (2016).
- Holz, C., Stuut, J.-B. W. & Henrich, R. Terrigenous sedimentation processes along the continental
margin off NW Africa: implications from grain-size analysis of seabed sediments. *Sedimentology* **51**,
1145-1154 (2004).
- 31 Drake, N. A., Blench, R. M., Armitage, S. J., Bristow, C. S. & White, K. H. Ancient watercourses and
biogeography of the Sahara explain the peopling of the desert. *Proceedings of the National Academy of
Sciences* **108**, 458-462 (2011).
- 32 Krastel, S. *et al.* CapTimiris Canyon: A newly discovered channel system offshore of Mauritania. *Eos,
Transactions American Geophysical Union* **85**, 417-423 (2004).
- 33 Zühlsdorff, C., Wien, K., Stuut, J. B. W. & Henrich, R. Late Quaternary sedimentation within a
submarine channel–levee system offshore Cap Timiris, Mauritania. *Marine Geology* **240**, 217-234
(2007).
- 34 Holz, C., Stuut, J.-B. W., Henrich, R. d. & Meggers, H. Variability in terrigenous sedimentation
processes off northwest Africa and its relation to climate changes: Inferences from grain-size
distributions of a Holocene marine sediment record. *Sedimentary Geology* **202**, 499-508 (2007).
- 35 Grousset, F. E. *et al.* Saharan wind regimes traced by the Sr–Nd isotopic composition of subtropical
composition of subtropical Atlantic sediments: Last Glacial Maximum vs today. *Quaternary Science
Reviews* **17**, 395-409 (1998).
- 36 McCave, I. N. Particulate size spectra, behavior, and origin of nepheloid layers over the Nova Scotian
Continental Rise. *Journal of Geophysical Research: Oceans* **88**, 7647-7666 (1983).
- 37 Gardner, W. D., Richardson, M. J. & Mishonov, A. V. Global assessment of benthic nepheloid layers
and linkage with upper ocean dynamics. *Earth and Planetary Science Letters* **482**, 126-134 (2018).
- 38 Biscaye, P. E. & Eittreim, S. L. Suspended particulate loads and transports in the nepheloid layer of the
abyssal Atlantic Ocean. *Marine Geology* **23**, 155-172 (1977).
- 39 Mulitza, S. *et al.* Increase in African dust flux at the onset of commercial agriculture in the Sahel region.
Nature **466**, 226-228 (2010).
- 40 Castillo, S. *et al.* Trace element variation in size-fractionated African desert dusts. *Journal of Arid
Environments* **72**, 1034-1045 (2008).
- 41 Skonieczny, C. *et al.* A three-year time series of mineral dust deposits on the West African margin:
Sedimentological and geochemical signatures and implications for interpretation of marine paleo-dust
records. *Earth and Planetary Science Letters* **364**, 145-156 (2013).
- 42 Meyer, I., Davies, G. R. & Stuut, J.-B. Grain size control on Sr-Nd isotope provenance studies and
impact on paleoclimate reconstructions: An example from deep-sea sediments offshore NW Africa.
Geochemistry, Geophysics, Geosystems **12**, Q03005 (2011).
- 43 Dasch, E. J. Strontium isotopes in weathering profiles, deep-sea sediments, and sedimentary rocks.
Geochimica et Cosmochimica Acta **33**, 1521-1552 (1969).
- 44 Aarons, S. M., Aciego, S. M. & Gleason, J. D. Variable HfSrNd radiogenic isotopic compositions in a
Saharan dust storm over the Atlantic: Implications for dust flux to oceans, ice sheets and the terrestrial
biosphere. *Chemical Geology* **349-350**, 18-26 (2013).
- 45 Zhao, W., Balsam, W., Williams, E., Long, X. & Ji, J. Sr–Nd–Hf isotopic fingerprinting of transatlantic
dust derived from North Africa. *Earth and Planetary Science Letters* **486**, 23-31 (2018).
- 46 Jewell, A. M. *et al.* Three North African dust source areas and their geochemical fingerprint. *Earth and
Planetary Science Letters* **554**, 116645 (2021).
- 47 Sarnthein, M. *et al.* in *Geology of the Northwest African Continental Margin* (eds Ulrich von Rad, Karl
Hinz, Michael Sarnthein, & Eugen Seibold) 545-604 (Springer Berlin Heidelberg, 1982).
- 48 Lever, A. & McCave, I. N. Eolian components in Cretaceous and Tertiary North Atlantic sediments.
Journal of Sedimentary Research **53**, 811-832 (1983).
- 49 Colin, C. *et al.* Late Miocene to early Pliocene climate variability off NW Africa (ODP 659).
Palaeogeography, Palaeoclimatology, Palaeoecology **401**, 81-95 (2014).
- 50 Vallé, F., Dupont, L. M., Leroy, S. A. G., Schefuß, E. & Wefer, G. Pliocene environmental change in
West Africa and the onset of strong NE trade winds (ODP Sites 659 and 658). *Palaeogeography,
Palaeoclimatology, Palaeoecology* **414**, 403-414 (2014).
- 51 Ruddiman, W. F. *et al.* in *Proceedings of the Ocean Drilling Program: Scientific Results*. Vol. 108
(ODP, 1989).
- 52 Zeeden, C. *et al.* Revised Miocene splice, astronomical tuning and calcareous plankton biochronology of
ODP Site 926 between 5 and 14.4 Ma. *Palaeogeography, Palaeoclimatology, Palaeoecology* **369**, 430-
451 (2013).

- 53 Krijgsman, W., Hilgen, F. J., Raffi, I., Sierro, F. J. & Wilson, D. S. Chronology, causes and progression
of the Messinian salinity crisis. *Nature* **400**, 652-655 (1999).
- 54 Mourik, A. A. *et al.* Astronomical tuning of the La Vedova High Cliff section (Ancona, Italy) –
Implications of the Middle Miocene Climate Transition for Mediterranean sapropel formation. *Earth
and Planetary Science Letters* **297**, 249-261 (2010).
- 55 Krijgsman, W., Fortuin, A. R., Hilgen, F. J. & Sierro, F. J. Astrochronology for the Messinian Sorbas
basin (SE Spain) and orbital (precessional) forcing for evaporite cyclicity. *Sedimentary Geology* **140**,
43-60 (2001).
- 56 van der Laan, E. *et al.* Astronomical forcing of Northwest African climate and glacial history during the
late Messinian (6.5–5.5 Ma). *Palaeogeography, Palaeoclimatology, Palaeoecology* **313–314**, 107-126
(2012).
- 57 Grinsted, A., Moore, J. C. & Jevrejeva, S. Application of the cross wavelet transform and wavelet
coherence to geophysical time series. *Nonlinear processes in geophysics* **11**, 561-566 (2004).
- 58 Manivit, H. in *Proceedings of the Ocean Drilling Program, Scientific Results, Vol.108* (ed W.
Ruddiman, Sarnthein, M., et al.,) 35-69 (ODP, 1989).
- 59 Schulz, M. & Mudelsee, M. REDFIT: estimating red-noise spectra directly from unevenly spaced
paleoclimatic time series. *Computers & Geosciences* **28**, 421-426 (2002).
- 60 Hammer, Ø., Harper, D. A. T. & Ryan, P. D. PAST: Paleontological Statistics Software Package for
Education and Data Analysis. *Palaeontologia Electronica* **4**, 9 (2001).
- 61 Lisiecki, L. E. & Raymo, M. E. A Pliocene-Pleistocene stack of 57 globally distributed benthic $\delta^{18}\text{O}$
records. *Paleoceanography* **20**, PA1003 (2005).
- 62 Tierney, J. E., deMenocal, P. B. & Zander, P. D. A climatic context for the out-of-Africa migration.
Geology **45**, 1023-1026 (2017).
- 63 deMenocal, P. B., Ruddiman, W. F. & Pokras, E. M. Influences of High- and Low-Latitude Processes on
African Terrestrial Climate: Pleistocene Eolian Records from Equatorial Atlantic Ocean Drilling
Program Site 663. *Paleoceanography* **8**, 209-242 (1993).
- 64 Pokras, E. M. & Mix, A. C. Earth's precession cycle and Quaternary climatic change in tropical Africa.
Nature **326**, 486-487 (1987).
- 65 Larrasoana, J. C., Roberts, A. P., Rohling, E. J., Winkelhofer, M. & Wehausen, R. Three million years of
monsoon variability over the northern Sahara. *Climate Dynamics* **21**, 689-698 (2003).
- 66 de Boer, B., Peters, M. & Lourens, L. J. The transient impact of the African monsoon on Plio-
Pleistocene Mediterranean sediments. *Clim. Past* **17**, 331-344 (2021).
- 67 Kutzbach, J. E. *et al.* African climate response to orbital and glacial forcing in 140,000-y simulation
with implications for early modern human environments. *Proceedings of the National Academy of
Sciences*, **117** (5), 2255-2264 (2020).
- 68 Bosmans, J. H. C., Hilgen, F. J., Tuenter, E. & Lourens, L. J. Obliquity forcing of low-latitude climate.
Clim. Past **11**, 1335-1346 (2015).
- 69 Schefuß, E., Rattmeyer, V., Stuut, J.-B. W., Jansen, J. H. F. & Sinninghe Damsté, J. S. Carbon isotope
analyses of n-alkanes in dust from the lower atmosphere over the central eastern Atlantic. *Geochimica et
Cosmochimica Acta* **67**, 1757-1767 (2003).
- 70 Eglinton, T. I. & Eglinton, G. Molecular proxies for paleoclimatology. *Earth and Planetary Science
Letters* **275**, 1-16 (2008).
- 71 Rommerskirchen, F. *et al.* A north to south transect of Holocene southeast Atlantic continental margin
sediments: Relationship between aerosol transport and compound-specific $\delta^{13}\text{C}$ land plant biomarker
and pollen records. *Geochemistry, Geophysics, Geosystems* **4** (2003).
- 72 Zhao, M., Dupont, L., Eglinton, G. & Teece, M. n-Alkane and pollen reconstruction of terrestrial
climate and vegetation for N.W. Africa over the last 160 kyr. *Organic Geochemistry* **34**, 131-143
(2003).
- 73 Hooghiemstra, H., Bechler, A. & Beug, H.-J. Isopollen maps for 18,000 years B.P. of the Atlantic
offshore of northwest Africa: Evidence for paleowind circulation. *Paleoceanography* **2**, 561-582 (1987).
- 74 Ehleringer, J. R. & Cerling, T. E. in *Global Biogeochemical Cycles in the Climate System* (eds Ernst-
Detlef Schulze *et al.*) 267-277 (Academic Press, 2001).
- 75 Huang, Y., Dupont, L., Sarnthein, M., Hayes, J. M. & Eglinton, G. Mapping of C4 plant input from
North West Africa into North East Atlantic sediments. *Geochimica et Cosmochimica Acta* **64**, 3505-
3513 (2000).
- 76 Niedermeyer, E. M. *et al.* Orbital- and millennial-scale changes in the hydrologic cycle and vegetation
in the western African Sahel: insights from individual plant wax δD and $\delta^{13}\text{C}$. *Quaternary Science
Reviews* **29**, 2996-3005 (2010).
- 77 Hoetzel, S., Dupont, L., Schefusz, E., Rommerskirchen, F. & Wefer, G. The role of fire in Miocene to
Pliocene C4 grassland and ecosystem evolution. *Nature Geosci* **6**, 1027-1030 (2013).
- 78 Feakins, S. J. *et al.* Northeast African vegetation change over 12 m.y. *Geology* **41** (3), 295–298 (2013).
- 79 Morley, R. J. & Richards, K. Gramineae cuticle: a key indicator of Late Cenozoic climatic change in the
Niger Delta. *Review of Palaeobotany and Palynology* **77**, 119-127 (1993).

- 80 Polissar, P. J., Rose, C., Uno, K. T., Phelps, S. R. & deMenocal, P. Synchronous rise of African C4
ecosystems 10 million years ago in the absence of aridification. *Nature Geoscience* **12**, 657-660 (2019).
- 81 Tierney, J. E., Russell, J. M. & Huang, Y. A molecular perspective on Late Quaternary climate and
vegetation change in the Lake Tanganyika basin, East Africa. *Quaternary Science Reviews* **29**, 787-800
(2010).
- 82 Beuning, K. R. M., Talbot, M. R., Livingstone, D. A. & Schmukler, G. Sensitivity of carbon isotopic
proxies to paleoclimatic forcing: A case study from Lake Bosumtwi, Ghana, over the last 32,000 years.
Global Biogeochemical Cycles **17**, 1121 (2003).
- 83 Sinninghe Damsté, J. S. *et al.* A 25,000-year record of climate-induced changes in lowland vegetation of
eastern equatorial Africa revealed by the stable carbon-isotopic composition of fossil plant leaf waxes.
Earth and Planetary Science Letters **302**, 236-246 (2011).
- 84 Lupien, R. L. *et al.* Vegetation change in the Baringo Basin, East Africa across the onset of Northern
Hemisphere glaciation 3.3–2.6 Ma. *Palaeogeography, Palaeoclimatology, Palaeoecology* **570**, 109426
(2021).
- 85 Lupien, R. L. *et al.* A leaf wax biomarker record of early Pleistocene hydroclimate from West Turkana,
Kenya. *Quaternary Science Reviews* **186**, 225-235 (2018).
- 86 Tierney, J. E. & deMenocal, P. B. Abrupt Shifts in Horn of Africa Hydroclimate Since the Last Glacial
Maximum. *Science* **342**, 843-846 (2013).
- 87 Feakins, S. J., Eglinton, T. I. & deMenocal, P. B. A comparison of biomarker records of northeast
African vegetation from lacustrine and marine sediments (ca. 3.40 Ma). *Organic Geochemistry* **38**,
1607-1624 (2007).
- 88 Castañeda, I. S. *et al.* Wet phases in the Sahara/Sahel region and human migration patterns in North
Africa. *Proceedings of the National Academy of Sciences* **106**, 20159-20163 (2009).
- 89 Badger, M. P. S. *et al.* CO₂ drawdown following the middle Miocene expansion of the Antarctic Ice
Sheet. *Paleoceanography* **28**, 42-53 (2013).
- 90 Badger, M. P. S. *et al.* Insensitivity of alkenone carbon isotopes to atmospheric CO₂ at low to moderate
CO₂ levels. *Clim. Past* **15**, 539-554 (2019).
- 91 Bartoli, G., Hönisch, B. & Zeebe, R. E. Atmospheric CO₂ decline during the Pliocene intensification of
Northern Hemisphere glaciations. *Paleoceanography* **26**, PA4213 (2011).
- 92 Bolton, C. T. *et al.* Decrease in coccolithophore calcification and CO₂ since the middle Miocene. *Nat
Commun* **7**, 10284 (2016).
- 93 Chalk, T. B. *et al.* Causes of ice age intensification across the Mid-Pleistocene Transition. *Proceedings
of the National Academy of Sciences* **114**, 13114 (2017).
- 94 de la Vega, E., Chalk, T. B., Wilson, P. A., Bysani, R. P. & Foster, G. L. Atmospheric CO₂ during the
Mid-Piacenzian Warm Period and the M2 glaciation. *Scientific Reports* **10**, 11002 (2020).
- 95 Dyez, K. A., Hönisch, B. & Schmidt, G. A. Early Pleistocene Obliquity-Scale pCO₂ Variability at ~1.5
Million Years Ago. *Paleoceanography and Paleoclimatology* **33**, 1270-1291 (2018).
- 96 Hönisch, B., Hemming, N. G., Archer, D., Siddall, M. & McManus, J. F. Atmospheric Carbon Dioxide
Concentration Across the Mid-Pleistocene Transition. *Science* **324**, 1551-1554 (2009).
- 97 Martinez-Boti, M. A. *et al.* Plio-Pleistocene climate sensitivity evaluated using high-resolution CO₂
records. *Nature* **518**, 49-54 (2015).
- 98 Pagani, M., Zachos, J. C., Freeman, K. H., Tipple, B. & Bohaty, S. Marked Decline in Atmospheric
Carbon Dioxide Concentrations During the Paleogene. *Science* **309**, 600-603 (2005).
- 99 Pagani, M., Liu, Z., LaRiviere, J. & Ravelo, A. C. High Earth-system climate sensitivity determined
from Pliocene carbon dioxide concentrations. *Nature Geoscience* **3**, 27 (2010).
- 100 Seki, O. *et al.* Alkenone and boron-based Pliocene pCO₂ records. *Earth and Planetary Science Letters*
292, 201-211 (2010).
- 101 Sosdian, S. M. *et al.* Constraining the evolution of Neogene ocean carbonate chemistry using the boron
isotope pH proxy. *Earth and Planetary Science Letters* **498**, 362-376 (2018).
- 102 Stap, L. B. *et al.* CO₂ over the past 5 million years: Continuous simulation and new $\delta^{11}\text{B}$ -based proxy
data. *Earth and Planetary Science Letters* **439**, 1-10 (2016).
- 103 Super, J. R. *et al.* North Atlantic temperature and pCO₂ coupling in the early-middle Miocene. *Geology*
46, 519-522 (2018).
- 104 Tanner, T., Hernández-Almeida, I., Drury, A. J., Guitián, J. & Stoll, H. Decreasing Atmospheric CO₂
During the Late Miocene Cooling. *Paleoceanography and Paleoclimatology* **35**, e2020PA003925
(2020).
- 105 Zhang, Y. G., Pagani, M., Liu, Z., Bohaty, S. M. & DeConto, R. A 40-million-year history of
atmospheric CO₂. *Philosophical Transactions of the Royal Society of London A: Mathematical,
Physical and Engineering Sciences* **371**, 20130096 (2013).
- 106 Zhang, Y. G., Pagani, M., Henderiks, J. & Ren, H. A long history of equatorial deep-water upwelling in
the Pacific Ocean. *Earth and Planetary Science Letters* **467**, 1-9 (2017).
- 107 Zhang, Y. G. *et al.* Refining the alkenone-pCO₂ method I: Lessons from the Quaternary glacial cycles.
Geochimica et Cosmochimica Acta **260**, 177-191 (2019).

- 108 Tauxe, L., Valet, J.-P. & Bloemendal, J. in *Proc. ODP, Sci. Results, 108* (ed W. Ruddiman, Sarnthein, M., et al.,) 429–439 (ODP, 1989).
- 109 Raffi, I. *et al.* A review of calcareous nannofossil astrobiochronology encompassing the past 25 million years. *Quaternary Science Reviews* **25**, 3113-3137 (2006).
- 110 Wade, B. S., Pearson, P. N., Berggren, W. A. & Pälike, H. Review and revision of Cenozoic tropical planktonic foraminiferal biostratigraphy and calibration to the geomagnetic polarity and astronomical time scale. *Earth-Science Reviews* **104**, 111-142 (2011).
- 111 Ogg, J. G. in *The Geologic Time Scale* (eds Felix M. Gradstein, James G. Ogg, Mark D. Schmitz, & Gabi M. Ogg) 85-113 (Elsevier, 2012).
- 112 Laskar, J. *et al.* A long-term numerical solution for the insolation quantities of the Earth. *Astronomy & Astrophysics* **428**, 261-285 (2004).